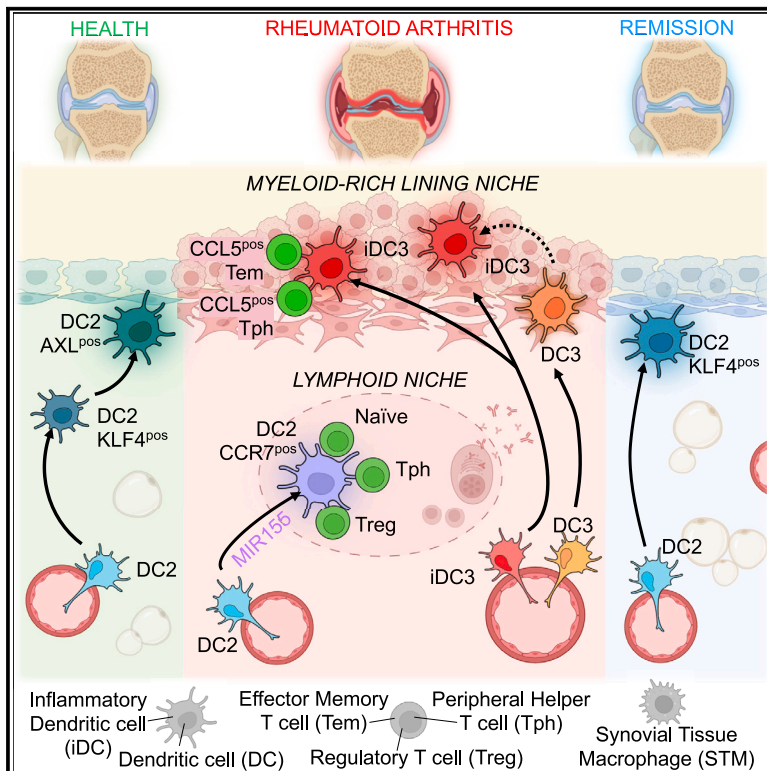# Immunity

Synovial tissue myeloid dendritic cell subsets exhibit distinct tissue-niche localization and function in health and rheumatoid arthritis

Graphical abstract

Authors

Lucy MacDonald, Aziza Elmesmari,
Domenico Somma, ..., Ilya Korsunsky,
Stefano Alivernini,
Mariola Kurowska-Stolarska

Correspondence

stefano.alivernini@unicatt.it (S.A.),
mariola.kurowska-stolarska@
glasgow.ac.uk (M.K.-S.)

In brief

How dendritic cells (DCs) regulate human tissue immunity remains unclear. MacDonald, Elmesmari, Somma, Frew, et al. investigate the role of synovial tissue (ST) myeloid DCs in health and active and remission stages of rheumatoid arthritis. Using a combination of scRNA-seq, spatial transcriptomics, and DC:T cell co-cultures, the authors identify functional features of ST-DCs that reveal their roles in immune tolerance and disease.

Highlights

- AXL+ DC2s with a tolerogenic phenotype reside beneath the healthy synovial lining

- iDC3s populate the hyperplastic lining in RA, activating Tem and/or Tph cells

- CCR7+ DC2s occupy sublining lymphoid niches in RA, interacting with naive T cells

- A signature of blood precursors of ST-DC3s predicts RA flare during remission

CellPress

Article

Synovial tissue myeloid dendritic cell subsets exhibit distinct tissue-niche localization and function in health and rheumatoid arthritis

Lucy MacDonald,[1,2,16] Aziza Elmesmari,[1,2,16] Domenico Somma,[1,2,16] Jack Frew,[1,2,16] Clara Di Mario,[3] Roopa Madhu,[4,5,6] Audrey Paoletti,[2] Theodoros Simakou,[1,2] Olympia M. Hardy,[1,2] Barbara Tolusso,[3] Denise Campobasso,[3] Simone Perniola,[3,7] Marco Gessi,[8] Maria Rita Gigante,[9] Luca Petricca,[9] Dario Bruno,[1,3,7] Lavinia Agra Coletto,[1,2,3] Roberta Benvenuto,[8] John D. Isaacs,[1,10,11] Andrew Filby,[12] David McDonald,[12] Jasmine P.X. Sim,[1,10] Nigel Jamieson,[13] Kevin Wei,[4] Maria Antonietta D'Agostino,[9] Neal L. Millar,[1,2] Simon Milling,[1,2] Charles McSharry,[2,14] Elisa Gremese,[1,3,7] Karen Affleck,[15] Kenneth F. Baker,[1,10,11] Iain B. McInnes,[1,2] Thomas D. Otto,[1,2] Ilya Korsunsky,[4,5,6] Stefano Alivernini,[1,2,3,9,16,*] and Mariola Kurowska-Stolarska[1,2,16,17,*]

[1]Research into Inflammatory Arthritis Centre Versus Arthritis (RACE), Glasgow, UK
[2]School of Infection & Immunity, University of Glasgow, Glasgow, UK
[3]Immunology Research Core Facility, Gemelli Science and Technology Park, Fondazione Policlinico Universitario A. Gemelli IRCCS, Rome, Italy
[4]Division of Rheumatology, Inflammation, and Immunity, Brigham and Women's Hospital and Harvard Medical School, Boston, MA 02115, USA
[5]Division of Genetics, Department of Medicine, Brigham and Women's Hospital, Boston, MA 02115, USA
[6]Broad Institute of MIT and Harvard, Cambridge, MA 02141, USA
[7]Division of Clinical Immunology, Fondazione Policlinico Universitario A. Gemelli IRCCS, Rome, Italy
[8]Institute of Pathology, Fondazione Policlinico Universitario A. Gemelli IRCCS, Rome, Italy
[9]Division of Rheumatology, Fondazione Policlinico Universitario A. Gemelli IRCCS, Rome, Italy
[10]Translational and Clinical Research Institute, Newcastle University, Newcastle upon Tyne, UK
[11]Musculoskeletal Unit, Newcastle-upon-Tyne Hospitals, Newcastle upon Tyne, UK
[12]Flow Cytometry Core Facility, Newcastle University, Newcastle upon Tyne, UK
[13]School of Cancer Sciences, University of Glasgow, Glasgow, UK
[14]NHS Greater Glasgow and Clyde, Glasgow, UK
[15]Respiratory and Immunology Research Unit, GSK, Stevenage, UK
[16]These authors contributed equally
[17]Lead contact
*Correspondence: stefano.alivernini@unicatt.it (S.A.), mariola.kurowska-stolarska@glasgow.ac.uk (M.K.-S.)
https://doi.org/10.1016/j.immuni.2024.11.004

SUMMARY

Current rheumatoid arthritis (RA) treatments do not restore immune tolerance. Investigating dendritic cell (DC) populations in human synovial tissue (ST) may reveal pathways to reinstate tolerance in RA. Using single-cell and spatial transcriptomics of ST biopsies, as well as co-culture systems, we identified condition- and niche-specific DC clusters with distinct functions. Healthy tissue contained tolerogenic AXL⁺ DC2s in the lining niche. In active RA, the hyperplasic lining niche was populated with inflammatory DC3s that activated CCL5-positive effector memory T cells, promoting synovitis. Lymphoid niches that emerged in the sublining layer were enriched with CCR7⁺ DC2s, which interacted with naive T cells, potentially driving the local expansion of new effector T cells. Remission saw the resolution of these pathogenic niches but lacked recovery of tolerogenic DC2s and exhibited activation of blood precursors of ST-DC3 clusters prior to flare-ups. Targeting pathogenic DC3s or restoring tolerogenic DC2s may help restore immune homeostasis in RA joints.

INTRODUCTION

Rheumatoid arthritis (RA) is an inflammatory joint disease with systemic comorbidities, driven by the breach of immune tolerance.[1] Advances in targeted therapies[2] have transformed the management of RA. However, 40% of RA patients still do not achieve lasting disease remission or a restored state of immunological homeostasis.[2–4] Drug-free remission is achieved in 10%–20% of RA patients, offering proof-of-concept that pathogenic innate-inflammatory and adaptive responses can be endogenously restrained.[3,5] However, even these patients exhibit persistence of autoimmunity, highlighting the absence of *immunological cure*.[6]

Dendritic cells (DCs) can reset the adaptive immune response and reinstate immune tolerance.[7] Thus, identifying DC phenotypes and their migration from peripheral blood (PB) to synovial tissue (ST) could help delineate their roles in immune tolerance
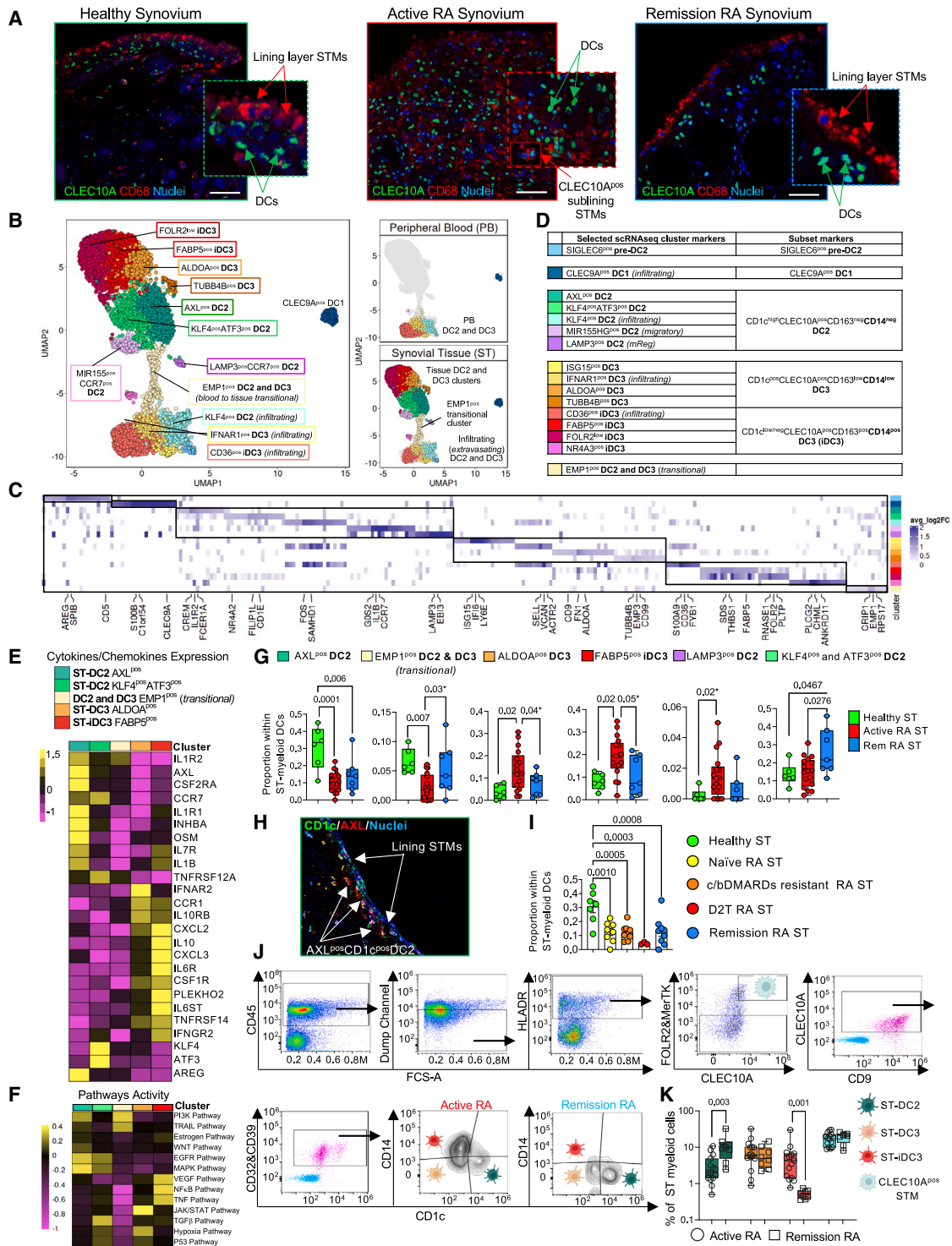
Figure 1. Single-cell omics identifies phenotypically distinct clusters of ST myeloid DC subsets

(A) Representative images showing immunofluorescence (IF) staining for myeloid DC markers, CLEC10A (green), CD68 (red), and nuclei DAPI (blue) in synovial tissues (STs). The inserts show cells at 40× magnification. Images are representative of ST from healthy donors (*n* = 5), active RA (*n* = 6), and remission RA (*n* = 5) from 3 independent experiments. Scale bars, 50 μm. Minimum and maximum display values for CLEC10A were set to 60 and 225, respectively, using QuPath (Version 0.4.2). DC, dendritic cell; STM, ST macrophage.

(B) Uniform manifold approximation and projection (UMAP) visualization of integrated CITE-seq (*n* = 7) and scRNA-seq (*n* = 35) data of myeloid DCs from ST and blood (PB) from 9 independent experiments. Each dot represents an individual cell. ST was obtained from healthy donors (*n* = 7), active RA (*n* = 18), remission RA (*n* = 9), and PB DCs from matched active RA (*n* = 3) and from healthy donors (*n* = 5).

(legend continued on next page)

and pathology. PB DC populations include plasmacytoid DCs (pDCs) and conventional DCs (cDCs).[8–11] The cDCs include DC1 (CD141^{pos}CLEC9A^{pos}) and two subsets of myeloid CLEC10A^{pos} DCs that differ in their bone marrow progenitors and their dominant transcription factors, now called DC2 and DC3, respectively.[8–10,12–15] PB DC2s are CD1c^{high}CLEC10A^{pos} CD163^{neg}CD14^{neg}, with a substantial proportion of cells expressing CD5 and B and T cell attenuator (BTLA), whereas PB DC3s are CD5^{neg}BTLA^{neg}CD1c^{low} and contain different phenotypic clusters that differ in the combination of CD163 and CD14 expression.[9,10] DC3s characterized by high expression of CD163 and CD14, show the greatest potential to activate Th2 and Th17 cells *in vitro*,[9,16] to support tumor cytotoxic CD8^{pos}CD103^{pos}CD69^{pos} tissue-resident memory T cells,[10] and to drive CD4^{pos} T cell immunity in experimental viral respiratory infections,[13] and, in this manuscript, they will be referred to as inflammatory DC3 (iDC3).

Functional DC atlases of diseased tissues[9,10,16–20] provided insight into the pathogenic role of discrete DC subsets and their tissue phenotypic states. For example, studies in cancer[21] led to the fine description of CCR7^{pos}LAMP3^{pos} mature DCs enriched in immunoregulatory molecules (mReg DC) as a molecular state (phenotype) acquired by both DC1 and DC2 subsets in tissue, which is associated with the induction of an immunogenic, regulatory, and migratory gene program,[21,22] depending on the surrounding environment.

Indirect evidence supports the role of ST-DCs in RA pathogenesis.[23–29] However, a comprehensive atlas of the functional diversity of ST-DCs is lacking. This study employed single-cell RNA sequencing (scRNA-seq), spatial transcriptomics, and ST-DC/T cell co-cultures to reveal the functional heterogeneity of synovial DCs, highlighting their roles in tissue immune tolerance and disease.

RESULTS

ST contains distinct phenotypic clusters of myeloid DCs

Our previous omic studies[30] revealed that, although healthy synovium has relatively low cellularity, it contains a population of myeloid CD1c^{pos}CLEC10A^{pos} DCs. Using immunofluorescent staining, we localized these cells below the protective lining layer of CD68^{pos}TREM2^{pos} ST macrophages (STMs).[30,31] In active RA, the distorted and hyperplastic lining layer contained an increased number of CLEC10A^{pos} DCs compared with healthy tissue. In remission, the structure of the lining layer and the number of DCs returned to a state resembling that of healthy individuals (Figure 1A; STAR Methods).

To identify DC subsets and their functional tissue phenotypes (clusters) in healthy and in discrete disease states, we performed scRNA-seq and cellular indexing of transcriptomes and protein epitopes sequencing (CITE-seq) on all cells or CD45^{pos} cells from ST biopsies of healthy donors (n = 7), active RA (n = 18), and RA in sustained disease remission (n = 9) (clinical data in Table S1). To guide annotation of ST-DCs, this was integrated with scRNA-seq from matched PB of active RA (n = 3) and healthy donors (n = 5) (Figure S1A; Table S2), where myeloid DC populations are well annotated.[9,12] This revealed ST-DCs that clustered together with blood cDCs (DC1 or DC2/DC3), suggesting that these are DCs that have just entered the tissue (infiltrating DCs) (Figure S1B). To identify all ST myeloid DCs, including those that acquire specific molecular states due to longer residency and activation in tissue, we also retained any other cell cluster that highly expressed HLADR and CD11c proteins, as well as CLEC10A mRNA (marker of myeloid DCs) (Figures S1C–S1F). This included three additional tissue clusters. The first, based on top myeloid DC2/3 markers (CLEC10A^{pos}, FCER1A^{pos}, HLADPB1^{pos}, and CD1c^{pos}), we temporarily called CLEC10A^{pos} NR4A3^{pos}CXCR4^{pos} tissue DCs (Figure S1G). The other two were subsets of STMs, FOLR2^{high}LYVE1^{pos}, which are perivascular macrophages[30,32] and FOLR2^{high}CLEC10A^{pos} STMs, exhibiting the strongest antigen-presenting cell transcriptomic profile among all STM subsets.[30] For the subsequent analysis, alongside the tissue CLEC10A^{pos}NR4A3[pos]CXCR4^{pos} DCs and infiltrating DCs, we retained the FOLR2^{high}CLEC10A^{pos} STMs and the blood/tissue monocyte clusters to exclude contamination of ST-DCs with any monocyte/macrophage cells. Re-clustering of these populations clearly separated transcriptomic profiles of

(C) Heatmap visualizing the average log fold change (logFC) of the top 5 marker genes of ST-DC clusters. Differentially expressed (DE) genes were determined using MAST and were considered significant if expressed in more than 40% of cells in the appropriate cluster with adjusted $p < 0.05$ after Bonferroni correction for multiple comparison. Average logFC $\geq$ 0.25.

(D) Table summarizing scRNA-seq markers of ST-DC subsets and their phenotypic clusters.

(E) Average-expression heatmap visualizing scaled expression of DE genes from the KEGG_cytokine/cytokine receptor pathway and selected cluster markers in ST myeloid DC clusters that differ between joint conditions (expressed in >25% of cells per cluster, with logFC > 0.5, and $p < 0.05$ in MAST with Bonferroni correction).

(F) Heatmap visualizing pathway activity across selected ST-DC clusters as in (E). Pathway activity based on top 500 genes per pathway from PROGENy database.

(G) Proportion of ST-DC2, DC3, and iDC3 clusters that differ between healthy controls, active RA, and remission RA (scRNA-seq). Data are presented as boxplot with a median and inter-quartile range. One-way ANOVA with Tukey corrections for multiple comparison, or two-sided Mann-Whitney (marked with *) if two groups were compared were used, the exact p values on the graphs.

(H) Representative image showing IF staining for CD1c (green), AXL (red), and nuclei (DAPI, blue) in healthy ST at 40× magnification. Images are representative of ST from healthy donors (n = 4) across 2 independent experiments. Scale bar, 50 μm.

(I) Difference in the proportion of ST AXL[pos] DC2 cluster within the ST-DC pool between healthy controls and different disease states of RA (scRNA-seq). Data are presented as a boxplot with median and inter-quartile range. One-way ANOVA with Tukey corrections, the exact p values on the graph. c/bDMARDs, conventional or biological disease-modifying anti-inflammatory drugs; D2T, difficult-to-treat. Each dot represents one patient.

(J and K) Multiparameter fluorescence-activated cell sorting (FACS) phenotyping of ST myeloid DC clusters guided by CITE-seq/scRNA-seq deconvolution. (J) Representative gating strategy for ST myeloid DC clusters from active RA and RA in remission.

(I) Percentage of ST myeloid DC clusters in total ST myeloid cells in active (n = 15) and remission RA (n = 8), across 10 independent experiments, presented as boxplot with a median and inter-quartile range. Two-sided Mann-Whitney, the exact p values on the graph.

See also Figures S1–S4 and Tables S1, S2, and S3.

tissue CLEC10A^pos^NR4A3^pos^CXCR4^pos^ DCs, infiltrating myeloid DC clusters and DC1s from monocytes and FOLR2^pos^ macrophages (Figures S1H and S1I). Subsequent unbiased re-clustering of only ST-DCs led to the identification of SIGLEC6^pos^ pre-DC2s, DC1s, and 14 myeloid DC clusters across healthy, active RA, and RA in remission synovium (Figures 1B–1D and S1J; Table S3). Although DC1s were reported to be abundant in RA synovial fluid,[27] and pre-DC2s were observed to increase during human skin inflammation,[33] they both constituted very small populations in ST and were not the focus of further analysis.

To aid annotation of myeloid DC clusters and determine from which PB DC subsets (DC2, DC3, and its iDC3 phenotype) each cluster differentiates, we next performed cell trajectory analysis (Figures S1K–S1M). RNA velocity, inferring trajectory from the direction of increased ratio of unspliced to spliced RNA counts (Figure S1K), supported by partition-based graph abstraction (PAGA) cell transition confidence evaluation (Figures S1L and S1M), identified 5, 5, and 4 distinct tissue phenotyping clusters maturing from PB DC2s, DC3s, and iDC3s, respectively (Figures 1B–1D). In summary, human ST contains a rich population of myeloid DCs.

Healthy ST contains the AXL^pos^ DC2 cluster
The 14 myeloid phenotypic clusters of DC2s, DC3s, and iDC3s (Figures 1B–1D) exhibited distinctive transcriptomes, characterized by differential expression of between 67 and 955 genes (Figure 1C; Tables S3 and S4). Identified clusters of the ST-DC2 subset expressed high mRNA for CD1c, lack of CD163 and CD14, and included (1) KLF4^pos^, (2) KLF4^pos^ATF3^pos^, (3) AXL^pos^, and two CCR7-positive clusters: (4) MIR155^pos^ and (5) LAMP3^pos^. Identified clusters of the ST-DC3 subset expressed CD163, and CD1c mRNA at a lower level, and included (1) IFNAR1^pos^, (2) ALDOA^pos^, (3) TUBB4B^pos^, and (4) ISG15^pos^. The ST-iDC3 expressed high mRNA for CD14 as compared with other DC3s and included (1) CD36^pos^, (2) FABP5^pos^, (3) NR4A3^pos^, and (4) FOLR2^low^ clusters (Figures 1D and S2).

ST KLF4^pos^ DC2, IFNAR1^pos^ DC3, and CD36^pos^ iDC3 represented an early tissue-infiltrating state of PB DC2s, DC3s, and iDC3s, respectively (Figure 1B). They exhibited a higher expression of integrins compared with their PB counterparts, which facilitate post-extravasation migration and maturation within the tissue,[34] including *ITGA10*, *ITGA11*, *ITGA5*, and *ITGB8* (Table S4). In addition, the matched PB/ST approach identified the EMP1^pos^ cluster, which might represent a subsequent transitional molecular state between infiltrating DCs and tissue-niche-specific DC phenotypic clusters (Figure 1B). This state, in contrast to other clusters, lacked the expression of cytokines and cytokine receptors (Figure 1E) but instead was enriched in the expression of genes encoding epithelial membrane proteins (EMPs) (Figures 1C and S2D; Table S3) and showed the activation signature of their downstream phosphatidylinositol 3-kinase (PI3K) pathway (Figure 1F), which is crucial for tumor cell invasiveness and tissue metastasis.[35]

Next, we deconvoluted the frequency of ST myeloid DC phenotypic clusters in different disease states and found substantial differences in AXL^pos^ DC2, EMP1^pos^ transitional DC2 and DC3, ALDOA^pos^ DC3, FABP5^pos^ iDC3, LAMP3^pos^ DC2 and KLF4^pos^ DC2 clusters between health, active RA, and RA in sustained remission (Figure 1G). In health, AXL^pos^ DC2s dominated, constituting approximately 40% of all DCs, whereas all other clusters

each constituted less than 5%–10% (Figure 1G) and represented the majority of DCs located under protective lining-layer TREM2^pos^ STMs (Figure 1H). The AXL^pos^ DC2 cluster was significantly decreased in active RA, especially in difficult-to-treat RA (Figure 1I), and was not reinstated in sustained remission. It exhibited regulatory features that include molecules important for local tissue homeostasis, such as *AXL*, an immune checkpoint that limits adaptive immune response,[28,36,37] amphiregulin (*AREG*), which is critical for tissue repair,[38] and inhibin beta A (*INHBA*), which is known for promoting an immunosuppressive environment.[39] It also exhibited molecular signatures reflecting activation of the tolerogenic WNT pathway[40] (Figures 1E, 1F, and S2E; Table S4). Cell trajectory analysis (Figure S1L; Table S3) showed that this AXL^pos^DC2 cluster likely developed from infiltrating KLF4^pos^ DC2s through an intermediate KLF4^pos^ATF3^pos^ stage.

Taken together, healthy ST is populated by a resident AXL^pos^ DC2 cluster that exhibits tolerogenic features likely crucial for maintaining local immune tolerance.

ST from active RA is enriched in iDC3s
In active RA synovium, we observed an increase in ALDOA^pos^ DC3 and FABP5^pos^ iDC3 phenotypic clusters compared with healthy tissue (Figure 1G). Cell trajectory analysis indicated that they develop from infiltrating CD14^pos^ DC3s (iDC3s) (Figure S1M). They together constitute more than 35% of RA ST-DCs and both shared transcriptomic profiles suggesting activation (Figure 1E). We observed an increased expression of *C15orf48* (Figure S2E; Table S4), a metabolic switch in complex I of the respiratory chain that we previously showed underlies the production of pro-inflammatory mediators by myeloid cells.[41]

In addition, ALDOA^pos^ DC3s and FABP5^pos^ iDC3s showed cluster-specific activation pathways. ST ALDOA^pos^ DC3s were distinguished by high expression of type I interferon (IFN) receptor (*IFNAR2*) (Figure 1E) and activation of the JAK/STAT pathway (Figure 1F).[14] ST FABP5^pos^ iDC3s had the highest expression of the high-affinity interleukin (IL)-6 receptor (*IL6R* and *IL6ST*) and tumor necrosis factor (TNF) receptor (*TNFRSF1B*), as well as activation of the TNF and NF-κB pathways (Figures 1E and 1F). We confirmed the presence of both DC3 and CD14^pos^ iDC3 phenotypes in a recently published ST scRNA-seq dataset of active RA[42] (Figure S2F).

In the remission ST, we observed a reduction in ALDOA^pos^ DC3s and FABP5^pos^ iDC3s compared with active RA. However, we noted a lack of restoration of the AXL^pos^ DC2 cluster that characterizes healthy tissue. Instead, we observed an increase in the proportion of its intermediate stages, namely infiltrating KLF4^pos^ and KLF4^pos^ATF3^pos^ DC2 clusters (Figure 1G). Transcriptomics of both suggest they progress toward regulatory function in remission tissue (Figures 1E, 1F, and S2E). For example, the infiltrating KLF4^pos^ cluster expressed *DUSP1* (Figure S2E), a key activator of IL-10,[43] whereas the ATF3^pos^ cluster expressed *VSIG4*, a PD-L1-like immune checkpoint that inhibits effector T cells[44] (Figure S2E). In addition, the ATF3^pos^ DC2 cluster showed activation of the tolerogenic transforming growth factor β (TGF-β) pathway (Figure 1F) and high expression of *ATF3* (Figure 1E), which are known for suppressing cytokine gene expression.[45] However, a lack of restoration of the AXL^pos^ phenotype potentially suggests an impaired tolerogenic state in remission synovium compared with health.
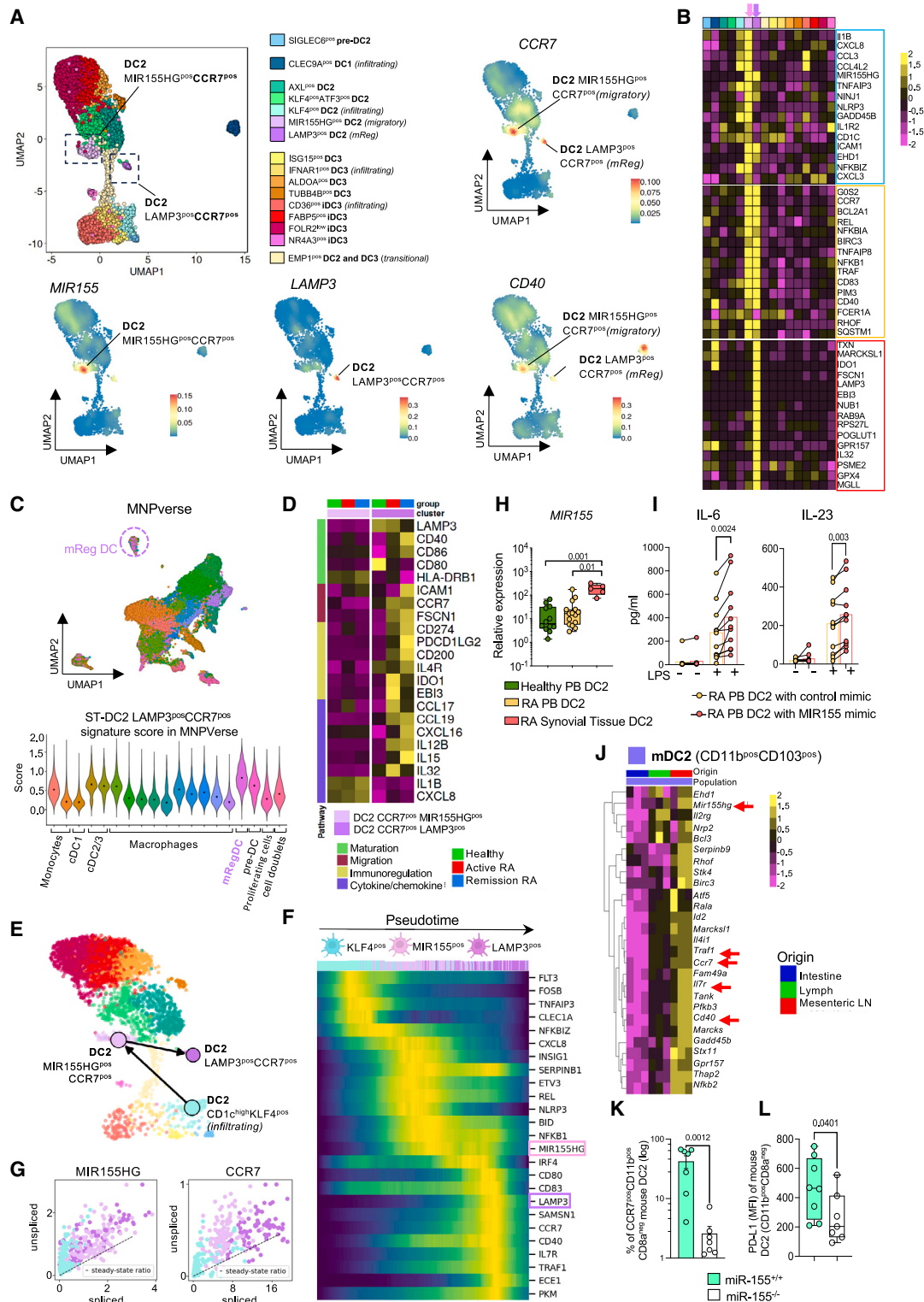
Figure 2. ST mReg DCs differentiate from activated MIR155^{pos}CCR7^{pos} intermediates in a process driven by MIR155

(A) UMAP visualization of integrated CITE-seq and scRNA-seq data of myeloid DCs from ST of healthy, active RA, and RA in disease remission as in Figure 1. Lines indicate two most-highly CCR7-expressing clusters: MIR155^{pos} and LAMP3^{pos}. Density plots illustrate expression of CCR7, MIR155, LAMP3, and CD40.

(legend continued on next page)

We next validated the frequency of ST-DC2 and DC3/iDC3 subsets by flow cytometry with additional synovial biopsies (n = 23). We found that canonical PB myeloid DC subset markers, such as CD5 or BTLA for DC2s, have limited expression in ST-DCs (Figures S1H and S2F). Thus, the specific gating of ST-DC subsets was guided by surface protein expression from ST CITE-seq data and previously identified markers of STM[30] (details in STAR Methods and Figures 1J and S3) and the accuracy confirmed with single-cell ST-DC index SORT-seq (Figure S4). This confirmed that remission tissues predominantly contained ST-DC2s (Figure 1K), whereas active RA was significantly enriched in cells of the CD14^{pos} iDC3 phenotype of DC3. Other DC3s were present in both, with a trend toward a higher contribution to the DC pool in active RA, consistent with our scRNA-seq data. Like our previous study,[30] the relative contribution of high-HLADR-expressing FOLR2^{pos}CLEC10A^{pos} STM macrophages to ST myeloid cells was comparable between active and remission tissues.

In summary, ST during RA pathology is enriched in iDC3 phenotypic clusters that resolve in remission RA.

ST from active RA is enriched in the LAMP3^{pos}CCR7^{pos} DC2 cluster

In active RA, although iDC3 clusters dominated the ST myeloid DC pool, the ST-DC2 population remained but showed notable changes compared with healthy individuals and those in remission. The AXL[pos] DC2 cluster was reduced, whereas CCR7^{pos}LAMP3^{pos} DC2s were increased (Figure 1G). We identified two CCR7-positive DC2 clusters co-expressing MIR155 and LAMP3, with one cluster showing higher MIR155 expression and the other higher LAMP3 expression (Figure 2A). Their high CCR7 suggests the potential for migration into draining lymph nodes (dLNs), where their high expression of the co-stimulatory molecule CD40 would enable them to activate naive T cells. They also shared high expression of nuclear factor (NF)-κB pathway genes (e.g., REL, TRAF1, and NFKB1), suggesting an activated

state (Figures 2A and 2B). MIR155 amplifies myeloid cell activation by inhibiting negative regulators of Toll-like receptor (TLR)/cytokine receptor signaling.[46] Consistent with this, high expression of pro-inflammatory mediators such as IL-1b and multiple chemokines were observed in the CCR7^{pos}MIR155^{high} DC2 cluster (Figure 2B). In contrast, the LAMP3^{pos} cluster exhibited IL-12, IL-15, and IL-32, together with increased expression of regulatory genes such as EBI3 (encoding a subunit of regulatory cytokines IL-27 and IL-35) and the immunomodulatory enzyme IDO1, the product of which is key for differentiation and activation of Treg cells (Figure 2B), thus resembling the recently identified mReg DC phenotype.[21] To investigate this, we integrated our ST single-cell dataset with a myeloid cell (MNP) single-cell RNA compendium (MNPVerse)[18] (Figure 2C; Table S4). Among all MNPVerse myeloid cells, the ST CCR7^{pos}LAMP3^{pos} DC2 signature scored highest with an MNPVerse mReg signature (Figure 2C), confirming that ST CCR7^{pos}LAMP3^{pos} DCs are indeed mReg. mReg are characterized by a unique immunogenic, regulatory, and migratory gene program.[21,47] Although the immunogenic program was increased in the LAMP3^{pos} DC2 cluster in both active and remission RA compared with health, the expression of some immunoregulatory genes, such as immune checkpoints (PDL-1 [CD274], PDL-2 [PDCD1LG2], and CD200), was increased in cells from remission tissue compared with those with active RA (Figure 2D). This suggests a distinct immunogenic versus regulatory program in active and remission RA, respectively.

To explore the relationship between MIR155^{pos} and mReg clusters in ST, we performed cell trajectory analysis. RNA velocity, aided by PAGA cell transition confidence evaluation (Figure 2E; Table S3), indicated that the ST CCR7^{pos}MIR155^{pos} cluster may constitute an intermediate stage of mReg DC2 differentiation from tissue-infiltrating KLF4^{pos} DC2s.

Next, to explore molecular mechanisms underlying the differentiation of the mReg DC2 from infiltrating KLF4^{pos} DC2s, we identified genes (Figures 2F and 2G) with a high ratio of unspliced

(B) Heatmap visualizing scaled top 15 unique marker genes of MIR155^{pos}CCR7^{pos} (blue box) and LAMP3^{pos}CCR7^{pos} (red box) DC2 clusters and the top 15 shared marker genes of these clusters (orange box) as compared with any other ST-DC cluster. Selection criteria: expressed >40% of cells in a cluster with logFC > 0.25 and p < 0.05 MAST with Bonferroni correction.

(C) Gene-set module score of ST LAMP3^{pos}CCR7^{pos} DC2 cluster (computed from their unique differentially expressed genes, STAR Methods) plotted across MNPVerse dataset (Mulder et al.[18]).

(D) Heatmap showing distinct expression of mReg DC genes identified by Maier et al.[21] in ST MIR155^{pos}CCR7^{pos} and LAMP3^{pos}CCR7^{pos} DC clusters between different joint conditions.

(E) Single-cell RNA velocity-directed PAGA showing differentiation trajectory of ST-DC2 LAMP3^{pos}CCR7^{pos} from tissue-infiltrating DC2s through the intermediate MIR155^{pos}CCR7^{pos} ST-DC2 stage (active RA n = 17).

(F) Pseudotime analysis of data from (E) shows candidate genes responsible for the maturation trajectory of ST-DC2 LAMP3^{pos}CCR7^{pos} from MIR155^{pos}CCR7^{pos} ST-DC2. Cells are colored by cluster identity and ordered by pseudotime.

(G) The ratio of newly transcribed (unspliced) pre-mRNA to spliced mRNA of MIR155 and CCR7 from KLF4^{pos} DC2s toward LAMP3^{pos} DC2s.

(H) Relative expression of MIR155 as compared with housekeeping microRNA (qPCR) in total CD1c^{high} DC2 population in PB of healthy donors (n = 12), PB of RA patients with active disease (n = 16), and from ST of RA patients with active disease (n = 5) across 10 independent experiments. Data are presented as boxplot with a median and inter-quartile range. One-way ANOVA with Tukey corrections, p values on the graph.

(I) Blood CD1c^{high} DC2s from active RA patients (n = 11, 10 independent experiments) transfected with miR-155 or control mimic (20 nM) and left unstimulated or stimulated with LPS (100 ng/mL). Production of cytokines is presented as paired dot plot with mean bars; each dot represents one patient. A paired t test, the exact p values on the graph.

(J) Heatmap showing log-normalized expression values of ST-DC2 LAMP3^{pos}CCR7^{pos} cluster markers significantly upregulated in bulk RNA-seq data of the mouse CD11b^{pos}CD103^{pos} myeloid DC2 cluster in lymph and mesenteric lymph nodes (mLNs) versus intestine tissue (n = 3 mice, 1 experiment) with p ≤ 0.05 (DESeq2 with Bonferroni correction). Red arrows point to the mReg gene score.

(K) The percentage of CCR7-expressing murine DC2s (CD11b^{pos}CD8a^{neg}) in mLN of WT (miR-155+/+, n = 7) and miR-155 deficient mice (miR-155−/−, n = 7) across 3 independent experiments. Data are presented as scatter dot plot with mean and SEM. Two-sided Mann-Whitney test, the exact p values on the graph.

(L) The MFI of PD-L1 expression by DC2s (CD11b^{pos}CD8a^{neg}) as in (K). Data are presented as boxplot with a median and inter-quartile range. Two-sided Mann-Whitney, p values on the graph.
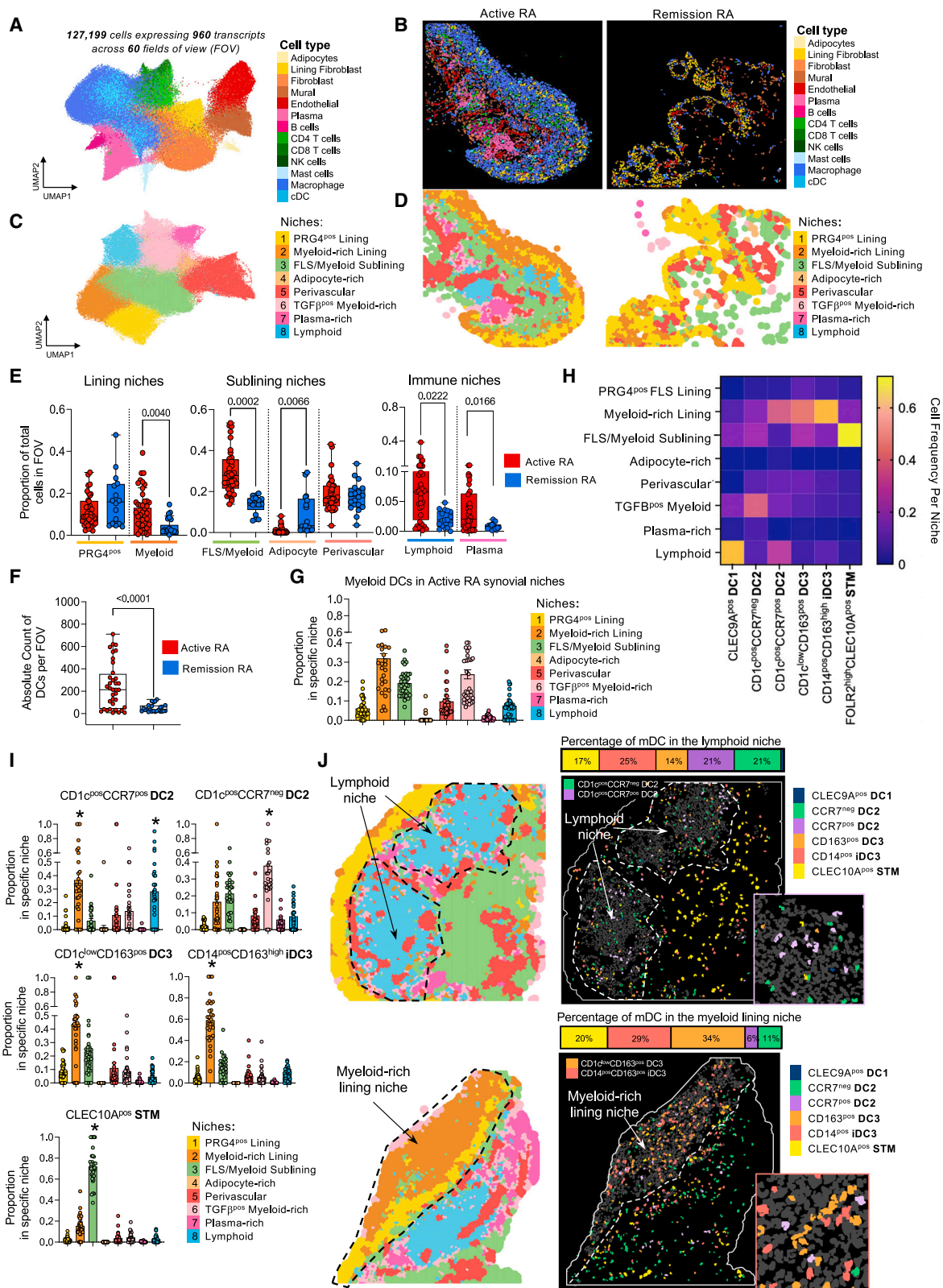
Figure 3. Different myeloid DC clusters localize in distinct ST niches

(A) UMAP visualization of clustering of coarse cell types identified from single-cell spatial transcriptomic data (CosMx, 960 gene panel) of 127,199 cells from $n = 69$ fields-of-view (FOVs) from ST of active RA ($n = 3$) and RA in remission ($n = 3$) across 3 experimental slides.

(legend continued on next page)

transcripts and differentially expressed (DE) along the pseudo-time of cell progression through the trajectory identified in Figure 2E. This highlighted MIR155 as (1) a potential driver of the highly pro-inflammatory state of the MIR155^pos cluster and (2) a candidate regulator of the migratory program of LAMP3^pos mReg. MIR155 expression was increased in the RA ST-DC2 cells as compared with PB counterparts (Figure 2H), suggesting its primary role in the local tissue maturation of infiltrating DC2s into an inflammatory MIR155^pos state. *In vitro* overexpression of MIR155 in PB DC2s from active RA significantly increased their production of IL-6 and IL-23 (Figure 2I), suggesting that MIR155 might govern the stimulatory functions of the CCR7^posMIR155^pos intermediate cluster in the synovium of patients with active RA.

Access to lymph and LN DCs in humans is challenging. To validate the migratory properties of the mReg and MIR155^pos clusters as closely as possible, we took advantage of a well-characterized mouse gut lymphatic cannulation model.[48] Using this model, we found that the mReg/MIR155^pos signature, including high expression of *Ccr7*, *mir155*, *Cd40*, and NF-κB pathway (*Traf1*), were significantly increased in mouse DC2s (CD11b^posC-D8a^neg) sorted from lymph and dLNs as compared with the matched tissue, confirming the LN migratory properties of these clusters (Figure 2J).

Along the mReg differentiation trajectory, high MIR155 expression occurred before CCR7 and other markers of the mReg DC2 (Figures 2F and 2G), indicating its role in the mReg migratory program. We found a significant decrease (~80%) in the proportion of CCR7^pos DC2 in the mesenteric LN of MIR155-deficient mice as compared with wild-type (WT) littermates (Figure 2K). These MIR155-deficient DC2 cells also had significantly less expression of another marker of mReg, PD-L1 (Figure 2L), confirming a key role of MIR155 in the regulation of mReg DC phenotype.

Taken together, these data suggest that active RA synovium contains an immunogenic mReg DC cluster, which differentiates from infiltrating DC2s through a highly activated CCR7^pos MIR155^pos intermediate stage.

Different myeloid DCs localize in distinct ST niches

To elucidate the function of distinct myeloid DC subsets/clusters in tissue, we next mapped their localization in ST niches and evaluated their interactions with specific T cell clusters. We performed single-cell spatial transcriptomics on ST biopsies from patients with active, treatment-naive RA and RA in disease remission (Figure S5A). To accurately identify cells within tissue, we used the Mesmer[49] and Baysor[50] methods, which estimate cellular edges based on nuclear staining and transcript densities, respectively. To deconvolute cell phenotype, we integrated spatial data with our reference single-cell omics datasets of those tissues (Figures 3A and 3B). A top marker gene correlation and confusion matrix confirmed accurate mapping of ST-DCs to the subset level (DC1, DC2, DC3, and iDC3 phenotypes) and the CCR7^pos DC2 (MIR155^pos/mReg) cluster level (Figures S5B and S5C).

First, we identified 8 distinct ST neighborhoods (niches) using Voronoi tessellation (STAR Methods; Figures 3C and 3D), each characterized by a distinct distribution of cell types and transcriptional signature (Figure S6; Table S3). These comprised two lining-layer niches: (1) *PRG4^pos niche*, dominated by PRG4-expressing lining-layer fibroblasts (FLS), and (2) the *myeloid-rich lining*, dominated by macrophages. Three structural sublining niches were identified and included: (1) *FLS/myeloid sublining niche*, enriched in interstitial macrophages and FLS; (2) *adipocyte-cell-rich niche*; and (3) *perivascular niche*, enriched in endothelial cells and pericytes. Three immune niches were identified: (1) enriched in T and B cells (*lymphoid niche*), which represent previously described RA synovium ectopic germinal centres[1,51]; (2) *plasma-cell-rich niche*; and (3) a niche enriched in regulatory TGF-β-expressing myeloid cells (*TGF-β-positive myeloid rich*). Active RA contained a larger myeloid-rich lining niche, lymphoid niche, and plasma-rich niche compared with remission. Conversely, remission exhibited a larger adipocyte-rich niche compared with active RA (Figure 3E).

Next, we investigated the distribution of different DC subsets within these niches. We mapped 8,887 DCs in active RA, with a median of 213 DCs per field of view (FOV). Due to the relative low cellularity of remission FOVs, we were only able to map 698 DCs across all remission FOVs, with a median number of 24 per FOV (Figure 3F). Therefore, in further analysis, we focused solely on the distribution of DC subsets within active RA niches. We found that DCs were particularly enriched in myeloid-rich lining, TGF-β^pos myeloid-rich sublining, myeloid/FLS sublining, and lymphoid niches (Figure 3G) and showed subtype-specific distribution (Figure 3H). CCR7^pos DC2s (mReg/MIR155^pos) were significantly enriched in the lymphoid niche, whereas the remaining DC2 (CCR7-negative) were in the TGF-β^pos myeloid-rich sublining niche. DC3 and its iDC3 phenotype were significantly

(B) Illustration of tissue single-cell segmentation and coarse cell-type annotation of representative FOVs from active RA and remission RA synovium.

(C) UMAP visualization of Louvain clustering of tiles from Voronoi tessellation of the tissue (details STAR Methods). Clusters represent regions (niches) from tissue segmentation that are annotated based on coarse cell-type composition and differential gene expression.

(D) Illustration of niche annotation of representative FOVs from active RA and remission RA synovium.

(E) Boxplots with a median and inter-quartile range showing the proportion of total cells in each FOV per identified niche in active RA (n = 36 FOVs, n = 3 patients) and in remission RA (n = 16 FOVs, n = 3 patients). Two-sided Mann-Whitney, the exact *p* values on the graph.

(F) Absolute number of myeloid DC clusters among all spatially mapped cells in active RA (n = 36) and Remission (n = 16) FOVs. Each dot represents one FOV. Data are presented as boxplot with a median and inter-quartile range. Two-sided Mann-Whitney, the exact *p* values on the graph.

(G) Distribution of ST myeloid DC clusters, DC1 and CLEC10A^pos STMs in different niches of active RA synovium. Each dot represents one FOV. Data are presented as the proportion of myeloid DCs per niche (bar plots with SEM).

(H) Heatmap summarizing the proportion of each myeloid DC cluster, DC1 and CLEC10A^pos STM per niche.

(I) Proportion of selected myeloid DC clusters per niche (bar plots with SEM). *$p < 0.01$ compared with any other niche (one-way ANOVA with Dunnett's corrections for multiple comparisons).

(J) Illustration of distinct distribution of ST-DC2 and DC3 and iDC3 clusters in lymphoid and lining myeloid-rich niches. The stack bar on the side shows the proportion of all myeloid DC clusters in those niches.

See also Figures S5 and S6 and Tables S2 and S3.
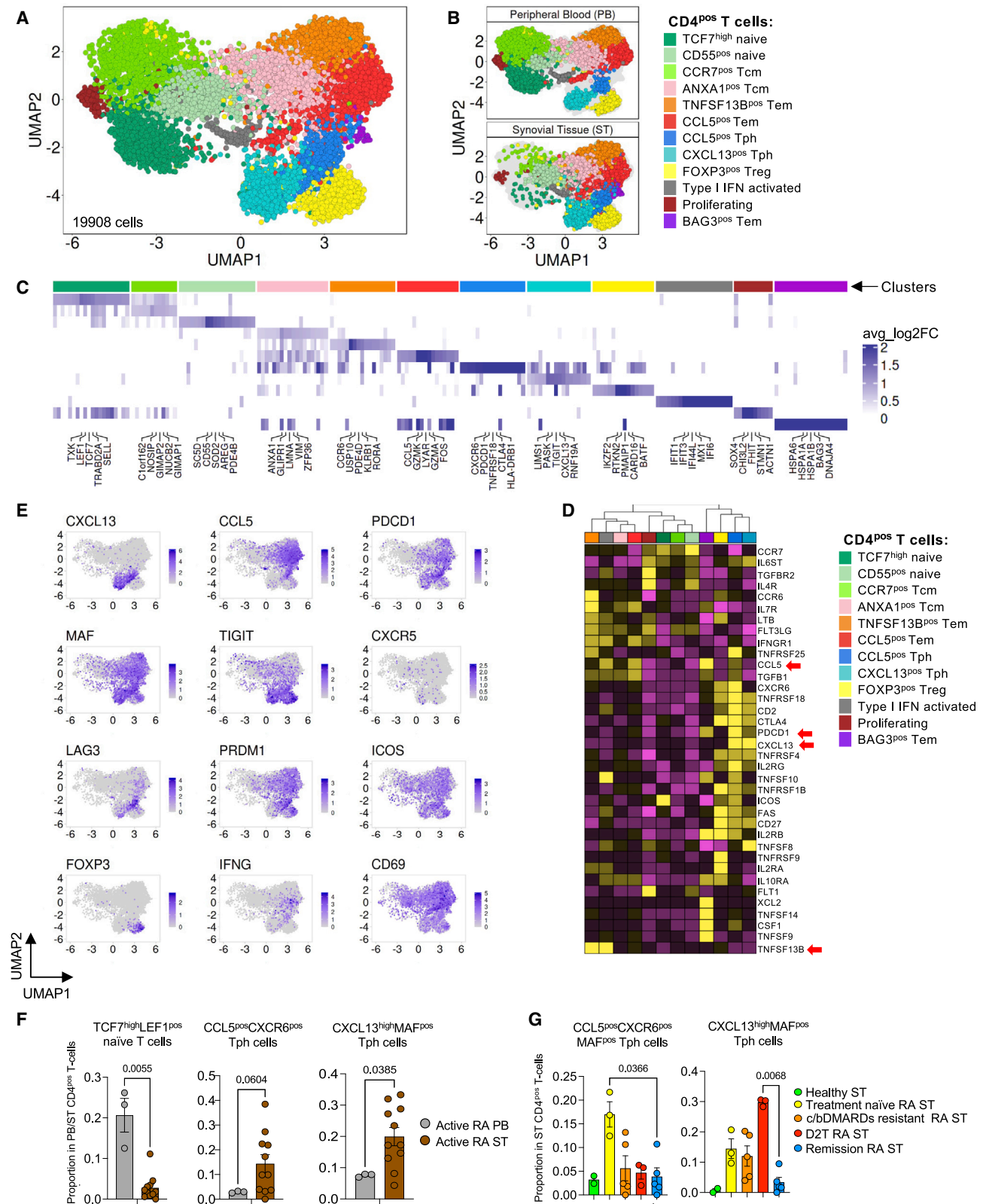
Figure 4. Distribution of CD4^{pos} T cell clusters in ST across different joint conditions

(A) UMAP visualization of integrated ST and PB CD4^{pos} T cell scRNA-seq data from ST of healthy ($n = 3$), active RA ($n = 12$), and RA in remission ($n = 5$) and from matched PB of active RA ($n = 3$) across 6 independent experiments.

(legend continued on next page)

enriched in the myeloid-rich lining niche (Figures 3I and 3J). In summary, ST-DC subsets exhibit tissue-niche-specific distribution, suggesting distinct local functions in regulating adaptive immunity.

Integrating DC and T cell subsets' biology in RA ST

To infer the function of mapped DC subsets in active RA tissue, we next mapped specific CD4^{pos} T cell synovial clusters. First, we deconvoluted ST T cell clusters across different disease stages, spanning from naive-to-treatment RA to difficult-to-treat RA and RA in disease remission using single-cell omics (Figure 4). Integration of these data with a dataset from matched blood aided allocation of naive versus memory status to the T cells. We identified twelve distinct CD4^{pos} T cell clusters: two naive T cell clusters and ten memory T cells, including two central memory (Tcm), six T effector memory (Tem), and Treg cell clusters. As expected, ST was enriched in memory cells with a small contribution of naive T cells, constituting less than 5% of the ST CD4^{pos} T cell pool. We integrated the ST part of this dataset with single-cell spatial transcriptomic data as in Figure 3 to accurately identify T cell clusters within the tissue (Figures S5D and S5E). As expected, active RA synovium was enriched in T cells (6,153 T cells, median of 137 per FOV) compared with remission (294 T cells, median of 12 per FOV) (Figure 5A).

Prior to investigating ST-DC subset interactions with T cell clusters in the tissue, we sought to uncover CD4^{pos} T cell phenotypes across the RA disease trajectory in our ST scRNA-seq dataset (Figures 4A–4E), providing deeper resolution to previously identified ST T cell clusters in RA.[42,52,53] Thus, we identified an additional phenotype of T peripheral helper (Tph) cell[54] that exhibits higher expression of Tph activation markers, such as *PD-1*, *LAG3*, and *PRDM1*, and high expression of *CCL5*, a potential key chemokine initiating joint flares,[53,55] in addition to the hallmark Tph cell cytokine *CXCL13*. The Tph cell phenotype characterized by CCL5 expression dominated in early naive-to-treatment RA, whereas the classical CXCL13^{pos}CCL5-negative Tph cells dominated in patients with persistent treatment-resistant synovitis (Figures 4F and 4G), suggesting potential evolution from acute CCL5-positive to classical Tph phenotype during disease progression. Another two large clusters of Tem cells in the active RA synovium included (1) cells expressing *TNFSF13B*, encoding B cell activating factor (BAFF) (RORA^{pos}TNFSF13B^{pos} cluster), which is a key survival factor for B cells.[56] (2) The second Tem cell cluster (CCL5^{pos}GZMA^{pos}) was distinguished by high expression of CCL5 (Figure 4E) and granzyme A (GZMA) (Figure 4C), a trigger of inflammatory mediators from tissue fibroblasts,[57] as well as IFN-γ, a driver of co-stimulatory molecule expression. This cluster was also characterized by high expres-

sion of *PD-1* and *CD69* (Figure 4E), altogether suggesting a highly activated pro-inflammatory Th1 cell state.

Next, neighborhood analysis inferred the T cell stimulatory functions of distinct ST-DC subsets by identifying which T cell phenotypes (clusters), described above, they interact with in tissue (see STAR Methods). The overall assessment of DC/T cell interactions in the synovium revealed a higher number of direct interactions (up to a distance of 40 μm, the diameter of a cell) between myeloid ST-DCs and CD4^{pos} T cells in active RA compared with remission RA tissues (Figure 5B). In active RA, we explored the interactions between specific ST-DC subsets and CD4^{pos} T cell clusters (Figures 5C and S6G) at two maximal distances: 40 μm to capture the initial DC-driven T cell phenotypes and 80 μm to capture potential daughter T cell phenotypes resulting from this interaction. This revealed that each ST-DC subset exhibited a distinct pattern of interactions with T cell clusters, implying varied T cell stimulatory functions. Overall, CCR7^{pos} DC2s (encompassing mReg and its MIR155^{pos} intermediate stage) and iDC3s showed the highest statistically significant associations with T cells, potentially indicating the most robust T cell stimulatory functions.

mReg DC2s interact with naive T cells in the ST lymphoid niche

Only mReg/MIR155^{pos} showed statistically significant interactions with naive T cells—and the most significant interactions with Treg cells among all DC subsets. Moreover, they exhibited the strongest interactions with BAFF-producing T cells (TNFSF13B^{pos}) and with CXCL13^{pos}CCL5^{neg} Tph cells, suggesting a role in the ectopic germinal center response in the synovium (Figure 5C). Histograms showing the number of interactions of CCR7^{pos} DC2s (mReg/MIR155^{pos}) with distinct T cell clusters at progressing distances confirmed the strongest interactions with naive T cells, Treg cells, and classical CXCL13^{pos} Tph in the lymphoid niche that represents ectopic germinal center (Figures 5D and 5E). Representative staining for mReg marker LAMP3 and spatial transcriptomic images of the lymphoid niche illustrated high frequency of mReg DCs in this niche and their close interactions with naive T cells, Treg cells, and classical CXCL13^{pos} Tph cells (Figures 5F–5H).

In summary, CCR7^{pos} (mReg/MIR155^{pos}) DCs, but not other DC subsets, interact with naive T cells in the lymphoid niche. Although these T cells constitute less than 5% of the total T cell population in the synovium, they are entirely located in this niche. The highly mature state of mReg/MIR155^{pos} DCs in this geographical location is likely responsible for driving naive T cells toward effector pathogenic function; for example, CXCL13^{pos} Tph cells *in situ*. Additionally, the regulatory gene

(B) Split UMAP visualizing data from PB versus ST.
(C) Heatmap illustrating ST T cell cluster markers (expressed in >40% of cells in a cluster, with logFC > 0.25, and p < 0.05, MAST with Bonferroni correction). Top 5 differentially expressed marker genes annotated based on greatest average logFC per cluster.
(D) Heatmap visualizing scaled differentially expressed genes from the KEGG cytokines and cytokine receptors pathway between different ST CD4^{pos} T cell clusters (criteria: expressed in >25% of cells per T cell cluster, with logFC > 0.5, and p < 0.05, MAST with Bonferroni correction).
(E) Expression of Tph cell and CCL5^{pos} Tem cell markers across ST CD4^{pos} T cell clusters.
(F) Bar plots (mean ± SEM) showing relative proportion of naive T cells and two Tph cell clusters in PB and ST CD4^{pos} T cell pool in active RA. Two-sided Mann-Whitney, the exact p values on the graph. Each dot represents healthy donor/patient.
(G) Bar plots (mean ± SEM) showing relative proportion of two Tph cell clusters in ST CD4^{pos} T cell pool across different joint conditions. One-way ANOVA with Dunn's correction, exact p values on the graphs. c/bDMARDs, conventional or biological disease-modifying anti-inflammatory drugs; D2T, difficult-to-treat. See also Figure S7 and Tables S2 and S3.
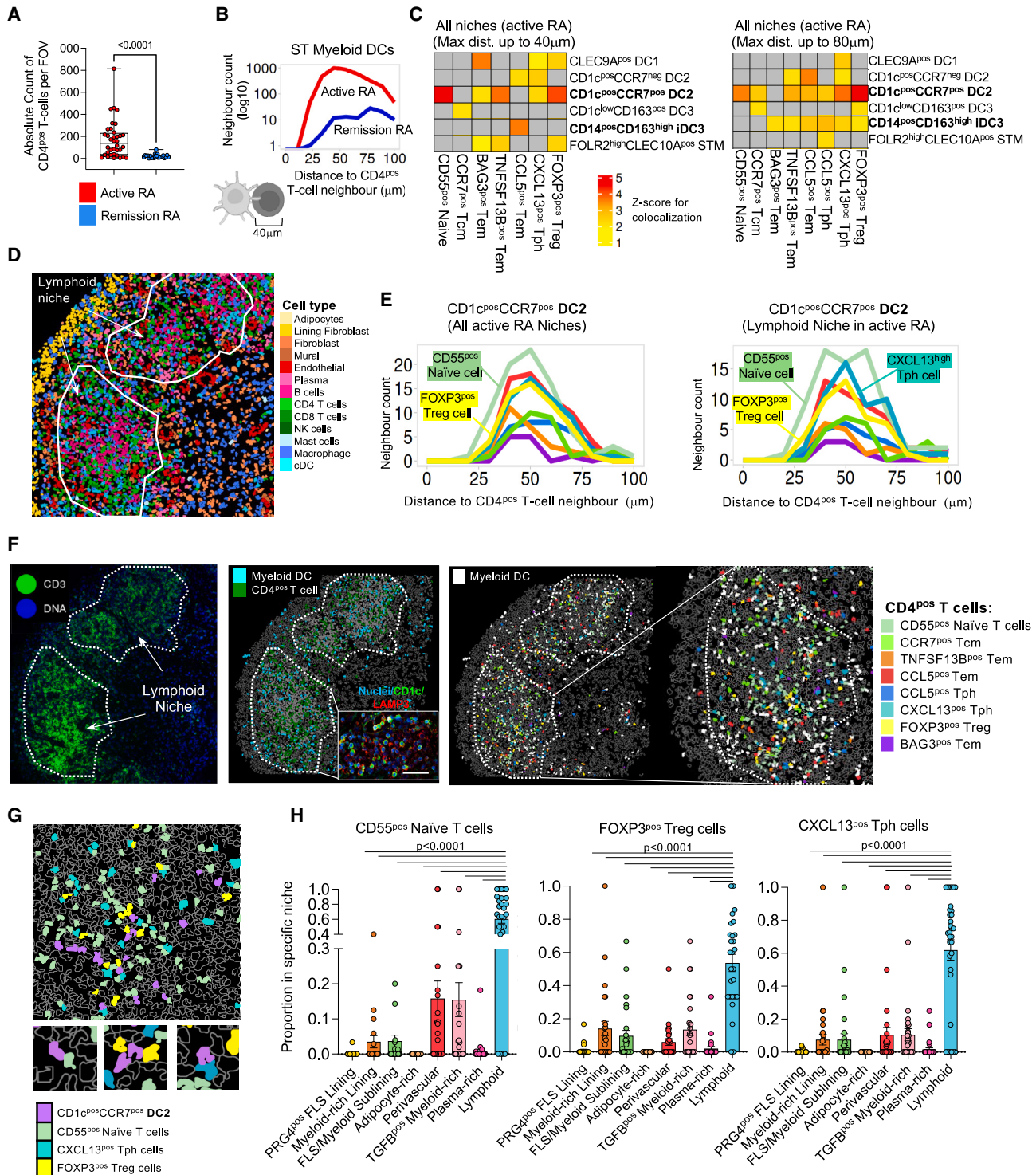
Figure 5. ST-DC subsets exhibit a different pattern of interactions with T cells in synovium

(A) Absolute number of ST CD4^{pos} T cells in all spatially mapped cells per FOV in active RA (n = 36 FOVs) and RA in remission (n = 16 FOVs) tissues as in Figure 3. Data are presented as a boxplot with median and inter-quartile range. Two-sided Mann-Whitney, the exact p values on the graph.

(B) Neighborhood analysis (see STAR Methods) showing direct (40 μm) and proximal (80 μm) interactions of myeloid DCs with CD4^{pos} T cells in active RA as compared with remission RA tissues. Number of FOVs as in (A).

(legend continued on next page)

program of mReg DCs likely underlies their strong interactions with Treg cells as part of an immune-response-induced negative feedback mechanism.

ST-iDC3s activate CCL5pos Tem and CCL5pos Tph cells in the synovial hyperplastic lining layer

The myeloid-rich hyperplastic lining layer is a unique feature of active RA synovium and a dominant niche for DC3s and their iDC3 phenotype (Figures 3I and 3J). Although at lower frequency than in lymphoid niches, the myeloid-rich lining-layer niche contained T cells, including highly activated CCL5pos Tph and CCL5pos Tem of Th1 cells (expressing *INF-γ*, *PD-1*, and *CD69*) (Figures 6A and 6B). Neighborhood analysis across all niches indicated that iDC3s preferentially interact directly (within 40 μm) with CCL5pos Tem cells compared with any other DC cluster (Figure 5C). Such interactions extend to CCL5pos Tph cells and, to a lesser extent, to other T cell clusters when examined over a wider 80-μm area, specifically in the myeloid-rich lining layer (Figures 5C, 6C, and 6D). Independent ligand-receptor analysis of our synovial scRNA-seq datasets confirmed statistically significant cellular interactions between ST-iDC3s and both CCL5pos Tem and CCL5pos Tph cells (Figure 6E) and identified the potential modes of communication between these subsets (Figure S7). The interactions of other DC3 phenotypes were limited to Tcm cells (Figure 4C), suggesting that these DC3s may maintain the reservoir of these long-lived cells in ST, whereas their iDC3 phenotype might play a prominent role in the activation of pathogenic CCL5pos Tem and CCL5pos Tph cell clusters.

To test whether ST-iDC3 drives the activation of CCL5pos T cells in active RA synovium, we established micro co-culture systems of synovial-biopsy-sorted DCs with autologous memory PB CD4pos T cells. We chose memory T cells because pathogenic memory CD4pos T cells appear in RA years before clinical symptoms, and their localization in the joints contributes to synovitis.[1] We included anti-CD3 antibody stimulation to mimic antigen-induced TCR engagement and assessed T cell activation using first scRNA-seq (Figures 6F–6H and S7A–S7C) and then flow cytometry (Figures 6I and 6J). We compared the T cell-stimulatory potential of patient-matched biopsy-sorted ST-iDC3s (CLEC10AposCD1clow/neg) to ST-DC2s (CLEC10AposCD1chigh). To accurately annotate the phenotypes of T cells that emerged from the co-cultures, we integrated the co-culture's scRNA-seq data with a reference ST memory CD4pos T cell's scRNA-seq dataset (Figure S7D). A local inverse Simpson's index

(LISI) score of 1.82, where 1 indicates no mixing and 2 indicates optimal mixing of *in vitro* and *in vivo* T cells, suggests a good degree of integration between co-cultured and tissue T cells (Figure S7F). Comparison of the T cell frequency between distinct co-culture conditions revealed a significant increase in the relative frequency of CCL5pos Tem cells in co-cultures with ST-iDC3s compared with those with patient's biopsy-matched ST-DC2s (Figures 6H and S7G). This increase was accompanied by enhanced expression of the activation marker ICOS in CCL5pos Tem cells (Figure S7H), whereas the expression of the proliferation marker *PCNA* and *TCF7* was comparable across different co-culture conditions (Figures S7I and S7J). These findings indicate that ST-iDC3s were more effective in activating CCL5pos Tem cells compared with ST-DC2s.

In synovial biopsies with sufficient ST-DCs, we used a rigorous CITE-seq-based and index-plate-sequencing-validated gating strategy to sort specific ST-DC subsets (Figures 1J, S3, and S4) and expanded our analysis of co-cultured T cells to include protein expression. PB memory CD4pos T cells were co-cultured with patient-matched ST-DC2s or ST-iDC3s in the presence of anti-CD3 antibody and IL-15 to provide an additional survival signal for memory T cells. Intracellular cytokine staining of T cells was used as a phenotypic readout for Tem (CCL5 and IFN-γ) and Tph (CCL5 and CXCL13) cells' activation at the end of the co-cultures. Both ST-DC2s and ST-DC3s enhanced anti-CD3-driven T cell activation, as evidenced by intracellular cytokine staining. However, ST-iDC3s were significantly more effective than biopsy-matched ST-DC2s in inducing CCL5, CXCL13, and IFN-γ production by PD1pos memory T cells (Figures 6I, 6J, and S7K). Additionally, CCL5-producing T cells co-cultured with ST-iDC3s showed higher expression of the activation marker CD69 and PD-1 compared with those co-cultured with ST-DC2s (Figure S7L), reminiscent of the CCL5pos Tem/Tph cell phenotypes found in tissue (Figure 4E). Taken together, these findings confirmed our tissue spatial transcriptomics and initial co-cultures, indicating that ST-iDC3s activate memory CCL5pos Tem and CCL5pos Tph cells.

To dissect the relationship between two CCL5pos T cell clusters driven by ST iDC3s, we conducted RNA velocity-based cell trajectory analysis on all ST CD4pos T cell clusters (Figure 6K). These data inferred that CCL5posCXCL13posTph cells can originate from CCL5pos Tem cells, providing an explanation for the colocalization of these two CCL5-positive T cell clusters with iDC3s in tissue and their synchronized increase in co-cultures with ST-iDC3s. This analysis also inferred the subsequent

---

(C) Neighborhood analysis of interactions between specific ST myeloid DC clusters, DC1 and CLEC10Apos STMs, and CD4pos T cells in active RA tissue. The direct (40 μm) and proximal (80 μm) interactions with CD4pos T cells that have significant *Z* scores are labeled with yellow-red colors, whereas insignificant ones are marked with gray (*n* = 36 FOVs in active RA).

(D) Coarse cell-type annotation in the lymphoid niche in representative FOVs from active RA synovium.

(E) Histograms illustrating the distances between CD1cposCCR7pos DC2s and CD4pos T cell clusters in all niches or specifically in the lymphoid niche.

(F) Representative images of the lymphoid niche from active RA tissue showing anti-CD3 immunofluorescence staining (green), followed by deconvolution of myeloid DC and T cell interactions, with specific T cell clusters identified by spatial transcriptomics (CosMx). Representative images of IF staining for CD1c (green), LAMP3 (red), and nuclei DAPI (blue) showing mReg DC in the lymphoid niche of synovium. This image is representative of ST from active RA (*n* = 6, 3 independent experiments). Scale bar, 20 μm.

(G) Representative image showing interactions of CD1cposCCR7posDC2 cells with FOXP3pos Treg cells, CD55posPDE4Bpos naive T cells, and CXCL13posMAFpos Tph cells in active RA ST based on spatial transcriptomic deconvolution.

(H) Proportion of T cell clusters that showed interactions with CD1cposCCR7pos DC2 cells in the lymphoid niche. Data are presented as a bar plot with SEM. One-way ANOVA with Dunnett's corrections, the exact *p* values on the graph.

See also Figures S5 and S6.
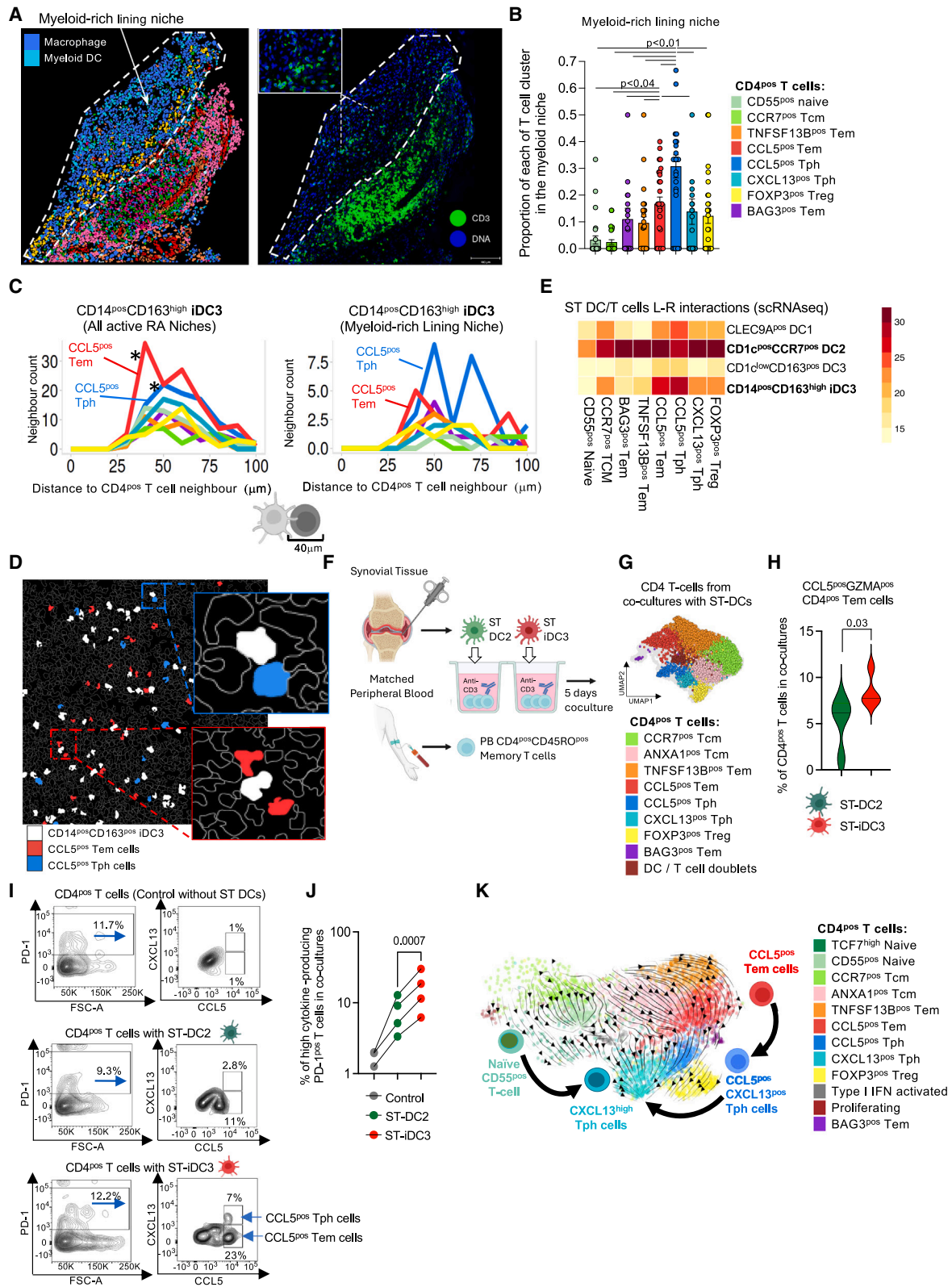
Figure 6. Synovial tissue iDC3s support CCL5^{pos} Tem/CCL5^{pos} Tph cells' activation

(A) Representative image of the myeloid-rich lining niche from active RA tissue identified by spatial transcriptomics, followed by the image of IF staining with anti-CD3 (green) in this niche as in Figure 3. Scale bar, 100 μm.

progression of CCL5^{pos} CXCL13^{pos} Tph to classical CXCL13^{pos} Tph cells, reflecting the progression in memory Tph phenotypes observed during the RA trajectory from early RA to chronic, difficult-to-treat disease (Figure 4G). Another notable developmental trajectory of CXCL13^{pos} Tph cells in the synovium is inferred from naive T cells. This accounts for the colocalization of naive T and CXCL13^{pos} Tph cells with mReg DC2s in the lymphoid niche. Together, these data indicate that ST-iDC3s are responsible for the activation of CCL5^{pos} Tem cells and their potential differentiation into CCL5^{pos} Tph cells in the hyperplastic, myeloid-rich synovial niche.

An inflammatory signature of PB iDC3s predicts disease flare in remission RA

To assess the contributions of distinct ST-DC subsets to the initiation of joint pathology, we examined the phenotypes of their blood predecessors in a human model of disease flare following treatment withdrawal (the BioRRA cohort[58,59]) (Figure 7A). In RA patients ($n = 12$) who achieved disease remission, we investigated the frequency and transcriptomic signature of PB DC1s, DC2s, and DC3s[9,10] at baseline (the time of treatment withdrawal) and at a second follow-up time point. This second time point was either at the occurrence of disease flare during the 6-month patient follow-up period (flare endpoint) or at the end of 6 months if the patient maintained drug-free remission (drug-free remission endpoint). The blood myeloid cell subsets and their phenotypes were deconvoluted with a 399-immune-gene panel in scRNA-seq (Figures 7B and 7C). Among the 12 patients investigated, 8 flared whereas 4 remained in drug-free remission after treatment withdrawal. The outcomes of flare or remission informed a categorical analysis of myeloid DC subsets at baseline and follow-up time points. We did not observe statistically significant differences in the frequencies of different PB DC subsets at baseline or at the time of disease flare (Table S4). However, comparison of their transcriptomic profiles at baseline revealed a pro-inflammatory gene signature (upregulation of expression of 33 genes) that distinguished patients who subsequently flared from those who would have remained

in remission. The upregulated expression of 24 of these pre-flare genes persisted in those patients predicted to flare to the onset of flare (Figure 7D). This gene panel include increased expression of integrins that facilitate migration into tissue (e.g., *ITGAM* and *ITGB2*), pattern recognition receptors (e.g., *TLR2* and *CLEC4E*), and alarmins (e.g., *S100A12*, *S100A9*, and *LGALS3*), suggesting an increased activation (Figure 7E). This pre-flare gene module was mostly confined to the PB iDC3 population (Figure 7F) and the ST-iDC3 clusters that mature from them in tissue (Figure 7G). This suggests that the activation of blood predecessors of ST-iDC3 clusters precedes pathology in the joint and supports their role in the initiation of synovitis, e.g., by driving the activation of CCL5-producing Tem/Tph cells in tissues.

In addition, receiver-operating characteristic curve (AUC-ROC) analysis of the pre-flare iDC3 gene module exhibited high sensitivity and specificity in stratifying these two remission outcome groups at baseline (Figure 7H). To verify this in an independent dataset, we investigated the expression of genes from the DC-flare-associated gene module across the weeks leading to flare and during flare in the longitudinal disease flare PRIMEcell study.[60] This dataset encompasses over 364 time points, both preceding and during eight flares, spanning a period of 4 years. We observed a fluctuating increase in the expression of the genes in our module starting 4 weeks before flare and persisting throughout the flare (Figure 7I), confirming the biomarker potential of the iDC3 signature in predicting disease flares.

DISCUSSION

This study delineated the heterogeneity and distinct functions of ST myeloid DCs, providing insights into mechanisms that might maintain tissue tolerance in health, drive autoimmunity in RA, or mediate flares during sustained remission.

We discovered that healthy ST contained, beneath the lining layer of TREM2^{pos} STM, a tissue-resident AXL^{pos} DC2 cluster with tolerogenic phenotype that likely differentiated from

(B) Distribution of CD4^{pos} T cell clusters in the myeloid-rich lining layer niche. Each dot represents one FOV ($n = 36$ active RA). Data are presented as the proportion of specific T cell clusters per this niche (bar plots with SEM). One-way ANOVA with Dunnett's corrections, the p values on the graph.

(C) Histograms illustrating the distances between ST-iDC3s and CD4^{pos} T cell clusters in all niches or specifically in the myeloid-rich lining niche (neighbor analysis of active RA FOVs as in Figure 5). Star represents interactions with significant Z score, as depicted in Figure 5C.

(D) Representative images showing interactions of ST-iDC3s with CCL5^{pos}GZMA^{pos} Tem cells and CCL5^{pos}CXCR6^{pos} Tph cells in active RA ST, based on spatial transcriptomic deconvolution.

(E) Heatmap showing the absolute number of predicted significant ($p < 0.05$) cellular interactions between T cell and DC subsets based on scRNA-seq data from Figure 1B (CellPhoneBD).

(F) DC2s and iDC3s were sorted from ST biopsies of patients with active RA (4 independent experiments) and co-cultured with autologous blood memory CD4^{pos} T cells for 5 days (details in STAR Methods).

(G) UMAP visualizing T cell phenotypes from the co-cultures with ST-DCs after integration of the co-culture scRNA-seq data with the ST T cell scRNA-seq data.

(H) Violin plot, displaying the median, depicts the percentage of CCL5^{pos}GZMA^{pos} Tem cells in co-cultures with synovial-biopsy-derived patient-matched ST-DC2s and ST-iDC3s. Data from 4 active RA synovial biopsies where both DC subsets were present. t test, p value on the graph. The number of successfully sequenced co-culture T cells ranged from 101 to 1,698.

(I) An example of surface PD-1 and intracellular CCL5 and CXCL13 protein expression by CD4^{pos} memory PB T cells co-cultured with autologous ST-DC2s or ST-iDC3s (sorted as in Figure S4) in the presence of anti-CD3 antibody (0.25 μg/mL) and IL-15 (20 ng/mL) or in the presence of anti-CD3 antibody (0.25 μg/mL) and IL-15 (20 ng/mL) only.

(J) Dot plot summarizing induction of cytokine production by PD-1^{pos} T cells co-cultured with patient-matched ST-DC2s and DC3/iDC3s ($n = 4$ RA). Paired t test, p value on the graph.

(K) Single-cell trajectory of ST CD4^{pos} T cells with RNA velocity analysis visualized on UMAP. The direction of arrows infers the path of cell trajectory based on spliced versus unspliced RNA counts.

See also Figure S7 and Table S3.
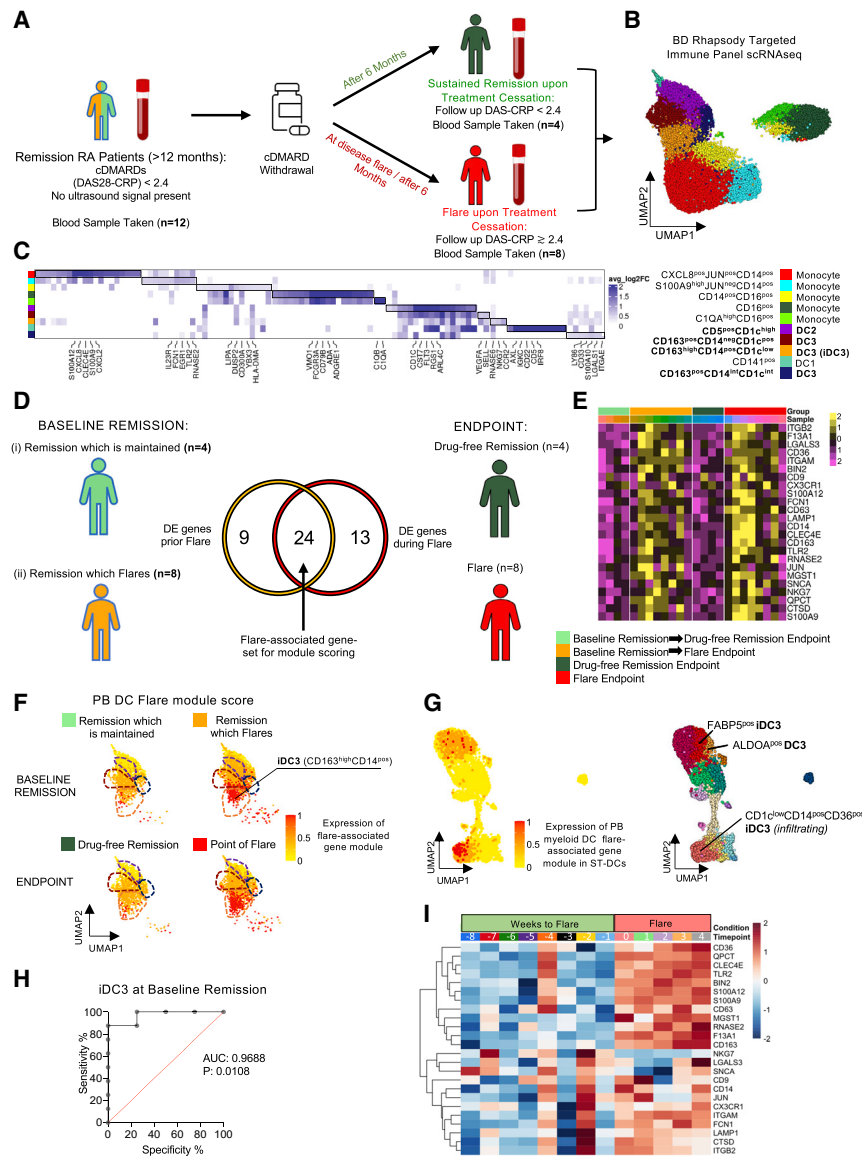
Figure 7. Transcriptomic profile of PB iDC3s of RA in remission is predictive of flare

(A) The layout of The Biomarkers of Remission in RA study (the BioRRA study). cDMARDs, conventional disease-modifying anti-rheumatic drugs.

(B) UMAP visualization of ten PB myeloid cell clusters identified in scRNA-seq analysis using an immune panel (399 genes).

(C) Heatmap illustrating the average logFC for genes identified as cluster markers (expressed in >40% of cells per cluster, with logFC > 0.25, and $p < 0.05$, MAST with Bonferroni correction). Top 5 differentially expressed marker genes annotated based on greatest average logFC per cluster.

(D) Schematic detailing flare-associated gene selection in myeloid dendritic cells (DC2, DC3, and its iDC3 phenotype) for preparation of DC-flare-associated gene module score. Venn diagram illustrates differentially expressed genes shared between baseline and end-point conditions (with logFC > 0.25, $p < 0.05$, Wilcoxon rank sum test with Bonferroni correction).

(E) Heatmap visualizing average scaled expression of 24 genes from the DC-flare-associated gene module score by sample and condition time points.

(F) UMAP visualization of the expression of PB myeloid DC-flare-associated gene module score by distinct PB DC subsets indicates the highest expression in PB iDC3s.

(G) UMAP visualization of the expression of PB myeloid DC-flare-associated gene module by ST myeloid DCs indicates the highest expression in ST-iDC3 clusters.

(H) Receiver-operating characteristic curves (ROC-AUCs) illustrate the performance of the average flare-associated module score at predicting flare upon treatment withdrawal at baseline in PB iDC3s.

(I) Heatmap visualizing mean scaled batch-corrected expression of genes from BioRRA flare-associated gene set across weeks relative to flare and during flare in the PRIME-cell dataset of disease flare (Orange et al.[60]). Data are generated from an index patient over 364 time points, both preceding and during eight flares, spanning a period of 4 years.

See also Tables S1 and S3.

infiltrating KLF4^pos DC2s. Together with inflammation-resolving TREM2^pos STMs,[30,31] they may comprise a myeloid innate system responsible for maintenance of ST immune homeostasis.

In the pathogenic tissue niches of active RA, a different phenotypic cluster of DC2s matured and iDC3s emerged. Infiltrating KLF4^pos DC2s differentiated into mReg DCs with a strong immunogenic and dLN migratory program, a process driven by MIR155. mReg DC2s and their highly activated CCR7^pos MIR155^pos intermediate stage localized within the ectopic lymphoid niches developing in the synovial sublining layer, where they likely induce the differentiation of naive T cells, specifically homing to this niche, into CXCL13^pos Tph cells, fueling the germinal center response in active RA synovitis. These interactions resemble those recently observed between mReg DCs and CXCL13^pos Tph cells in liver and lung tumor niches.[54,61] In addition, the hyperplastic aberrant lining layer that develops from inflammatory subsets of MerTK^neg macrophages and replaces the protective TREM2^pos

STM[30,62] became the niche for a highly activated tissue FABP5^pos phenotype of the iDC3 cluster. The iDC3s activated infiltrating memory CCL5^pos Tem cells and induced their differentiation into CCL5^pos CXCL13^pos Tph cells that characterize early synovitis and are predicted to differentiate into the classical CXCL13^pos cells that dominate in later disease stages. Study of drug-free remission RA demonstrated that a pro-inflammatory gene module characterizing tissue iDC3s appeared in a PB iDC3 cluster prior to flare onset. This finding, together with a recent report showing an increase in CCL5^pos Tem cells (GZMA^pos) at the onset of flare,[59] supports the potential role of the iDC3-CCL5^pos Tem/Tph cell axis as a critical initiating step in localizing immune responses in joints. This suggests that iDC3-memory CCL5^pos Tph might drive early synovitis and mediate progression from a myeloid to a lymphoid pathotype[1,63] with ectopic germinal centers homing autoreactive naive T cells, leading to *in situ* development of Tph cells driven by mReg/MIR155^pos DC2s. Studies

with longitudinal ST biopsies, spanning from pre-clinical RA to onset of arthritis, are needed to validate this hypothesis.

In sustained disease remission, RA ST exhibited the resolution of the hyperplastic myeloid-rich lining, as well as lymphoid niches in the sublining, and showed the restoration of a protective TREM2-positive STM lining layer.[62] This was accompanied by a decrease in the frequency of iDC3s and restoration of DC2s beneath the lining layer, resembling the structure of healthy synovium. However, these cells did not fully acquire the AXL[pos] DC2 tolerogenic program characteristic of healthy tissue. Instead, they stalled at a predicted intermediate stage, KLF4^{pos}ATF3^{pos} DC2s, showing the restoration of only some, but not all, of the tolerogenic potential characteristic of healthy tissue DC2s. This suggests a latent potential for disease flare in the joints of patients in remission. Plausible mechanisms preventing the acquisition of the AXL[pos] tolerogenic DC2 phenotype in remission tissue remain to be investigated and may include epigenetic changes in their bone marrow precursors and/or the tissue niches, both as a result of prior chronic inflammation.

In summary, our data suggest that therapeutic strategies to block the pathogenic functions of ST-iDC3s and reinstate the tolerogenic functions of the ST AXL[pos] DC2 cluster might be the necessary step-change for resolution of synovitis and transition from remission into self-maintained immune homeostasis.

Limitations of the study
The main limitation of this study is the lack of functional insight into how ST-DC subsets regulate RA autoantigen-specific naive T cells, compounded by the extremely low frequency of such T cells in the PB of RA patients.[64]

RESOURCE AVAILABILITY

Lead contact
Further information and requests for resources and reagents should be directed to and will be fulfilled by the lead contact, Mariola Kurowska-Stolarska (mariola.kurowska-stolarska@glasgow.ac.uk).

Materials availability
This study did not generate new unique reagents.

Data and code availability
All scRNA-seq and spatial data raw files are available from ArrayExpress under accession numbers E-MTAB-14191 (Co-Culture scRNA-seq), E-MTAB-14169 (BioRRA scRNA-seq), E-MTAB-14192 (Paired PB/ST scRNA-seq), E-MTAB-14213 (healthy, active RA and remission ST scRNA-seq/CITE-seq), E-MTAB-14198 (Sort-seq), S-BSST1483 (CosMx Spatial Transcriptomics). Scripts for analysis of scRNA-seq and published bulk RNA-seq datasets are available at https://doi.org/10.5281/zenodo.13866418. All raw microscopy pictures are available at BioImage Archive under accession number S-BIAD1388. More details are provided in the key resources table. All original code (Spatial Transcriptomic Data Analysis) has been deposited at Zenodo repository and is publicly available at https://doi.org/10.5281/zenodo.13869471 as of date of publication. Any additional information required to re-analyze the data reported in this paper is available from the lead contact upon request.

AUTHOR CONTRIBUTIONS

Conceptualization, M.K.-S., L.M., A.E., D.S., J.F., and S.A.; methodology, A.E., L.M., D.S., and J.F.; software, L.M., R.M., K.W., I.K., and D.S.; formal analysis, L.M., D.S., A.E., J.F., A.P., O.M.H., T.S., B.T., C.D.M., D.C., R.B., M.G., S.A., and M.K.-S.; investigation, A.E., L.M., D.S., J.F., and A.P.; resources, S.A., E.G., M.R.G., S.P., D.B., M.A.D'A., L.P., L.A.C., N.L.M., K.F.B., J.D.I., A.F., D.M., J.P.X.S., and S.M.; data curation, L.M., D.S., and J.F.; writing, M.K.-S., L.M., A.E., J.F., D.S., and S.A.; visualization, L.M., J.F., A.E., D.S., S.A., and M.K.-S.; assistance with data interpretation, C.M., E.G., K.A., I.B.M., and T.D.O.; supervision, project administration, and funding acquisition, M.K.-S. and S.A.

DECLARATION OF INTERESTS

The authors declare no competing interests.

STAR★METHODS

Detailed methods are provided in the online version of this paper and include the following:

- KEY RESOURCES TABLE
- EXPERIMENTAL MODEL AND STUDY PARTICIPANTS
  - Human participants
  - Animals
- METHOD DETAILS
  - Semiquantitative histological assessment of synovitis degree
  - Sample preparation for single cell RNAseq and CITEseq of peripheral blood and ST
  - ST-DC index SORT-seq, flow cytometry evaluation of ST-DC subsets' frequency and sorting for the co-cultures with autologous T cells
  - ST-DC/T cells Co-cultures
  - Mapping DC subsets in STs using immunofluorescent staining
  - The *in vivo* model of disease flare in remission RA
  - Sample Preparation for BD Rhapsody scRNAseq of DC-T Co-Culture_1 and BioRRA Cohort and PB DCs
  - Analysis of all Single Cell RNA Sequencing Data
  - MNP-Verse analysis
  - Mapping of ST myeloid DC in situ with CosMx single cell spatial transcriptomics
  - Niche and colocalization analysis of CosMx spatial transcriptomic data
  - Dimension reduction and clustering
  - PRIME cells data set analysis
  - MIR155 expression and experimental overexpression of MIR155 in ex-vivo peripheral blood (PB) DC2 cells
  - Phenotyping DCs in mesenteric lymph nodes (mLN) in wild type and miR-155 gene deficient mice
  - Isolation and analysis of mouse DC2 from gut, lymph and draining lymph nodes
- QUANTIFICATION AND STATISTICAL ANALYSIS

REFERENCES

1. Alivernini, S., Firestein, G.S., and McInnes, I.B. (2022). The pathogenesis of rheumatoid arthritis. Immunity 55, 2255–2270. https://doi.org/10.1016/j.immuni.2022.11.009.

2. Schett, G., McInnes, I.B., and Neurath, M.F. (2021). Reframing immune-mediated inflammatory diseases through signature cytokine hubs. N. Engl. J. Med. 385, 628–639. https://doi.org/10.1056/NEJMra1909094.

3. Aletaha, D., and Smolen, J.S. (2018). Diagnosis and management of rheumatoid arthritis: a review. JAMA 320, 1360–1372. https://doi.org/10.1001/jama.2018.13103.

4. Jansen, D.T.S.L., Emery, P., Smolen, J.S., Westhovens, R., Le Bars, M., Connolly, S.E., Ye, J., Toes, R.E.M., and Huizinga, T.W.J. (2018). Conversion to seronegative status after abatacept treatment in patients with early and poor prognostic rheumatoid arthritis is associated with better radiographic outcomes and sustained remission: post hoc analysis of the AGREE study. RMD Open 4, e000564. https://doi.org/10.1136/rmdopen-2017-000564.

5. Smolen, J.S., Landewé, R.B.M., Bergstra, S.A., Kerschbaumer, A., Sepriano, A., Aletaha, D., Caporali, R., Edwards, C.J., Hyrich, K.L., Pope, J.E., et al. (2023). EULAR recommendations for the management of rheumatoid arthritis with synthetic and biological disease-modifying antirheumatic drugs: 2022 update. Ann. Rheum. Dis. 82, 3–18. https://doi.org/10.1136/ard-2022-223356.

6. de Moel, E.C., Derksen, V.F.A.M., Trouw, L.A., Bang, H., Goekoop-Ruiterman, Y.P.M., Steup-Beekman, G.M., Huizinga, T.W.J., Allaart, C.F., Toes, R.E.M., and van der Woude, D. (2018). In RA, becoming seronegative over the first year of treatment does not translate to better chances of drug-free remission. Ann. Rheum. Dis. 77, 1836–1838. https://doi.org/10.1136/annrheumdis-2018-213823.

7. Banchereau, J., and Steinman, R.M. (1998). Dendritic cells and the control of immunity. Nature 392, 245–252. https://doi.org/10.1038/32588.

8. Villani, A.C., Satija, R., Reynolds, G., Sarkizova, S., Shekhar, K., Fletcher, J., Griesbeck, M., Butler, A., Zheng, S., Lazo, S., et al. (2017). Single-cell RNA-seq reveals new types of human blood dendritic cells, monocytes, and progenitors. Science 356, eaah4573. https://doi.org/10.1126/science.aah4573.

9. Dutertre, C.A., Becht, E., Irac, S.E., Khalilnezhad, A., Narang, V., Khalilnezhad, S., Ng, P.Y., van den Hoogen, L.L., Leong, J.Y., Lee, B., et al. (2019). Single-cell analysis of human mononuclear phagocytes reveals subset-defining markers and identifies circulating inflammatory dendritic cells. Immunity 51, 573–589.e8. https://doi.org/10.1016/j.immuni.2019.08.008.

10. Bourdely, P., Anselmi, G., Vaivode, K., Ramos, R.N., Missolo-Koussou, Y., Hidalgo, S., Tosello, J., Nuñez, N., Richer, W., Vincent-Salomon, A., et al. (2020). Transcriptional and functional analysis of CD1c(+) human dendritic cells identifies a CD163(+) subset priming CD8(+)CD103(+) T cells. Immunity 53, 335–352.e8. https://doi.org/10.1016/j.immuni.2020.06.002.

11. Brown, C.C., Gudjonson, H., Pritykin, Y., Deep, D., Lavallée, V.P., Mendoza, A., Fromme, R., Mazutis, L., Ariyan, C., Leslie, C., et al. (2019). Transcriptional basis of mouse and human dendritic cell heterogeneity. Cell 179, 846–863.e24. https://doi.org/10.1016/j.cell.2019.09.035.

12. Cytlak, U., Resteu, A., Pagan, S., Green, K., Milne, P., Maisuria, S., McDonald, D., Hulme, G., Filby, A., Carpenter, B., et al. (2020). Differential IRF8 transcription factor requirement defines two pathways of dendritic cell development in humans. Immunity 53, 353–370.e8. https://doi.org/10.1016/j.immuni.2020.07.003.

13. Bosteels, C., Neyt, K., Vanheerswynghels, M., van Helden, M.J., Sichien, D., Debeuf, N., De Prijck, S., Bosteels, V., Vandamme, N., Martens, L., et al. (2020). Inflammatory Type 2 cDCs acquire features of cDC1s and macrophages to orchestrate immunity to respiratory virus Infection. Immunity 52, 1039–1056.e9. https://doi.org/10.1016/j.immuni.2020.04.005.

14. Girard, M., Law, J.C., Edilova, M.I., and Watts, T.H. (2020). Type I interferons drive the maturation of human DC3s with a distinct costimulatory profile characterized by high GITRL. Sci. Immunol. 5, eabe0347. https://doi.org/10.1126/sciimmunol.abe0347.

15. Liu, Z., Wang, H., Li, Z., Dress, R.J., Zhu, Y., Zhang, S., De Feo, D., Kong, W.T., Cai, P., Shin, A., et al. (2023). Dendritic cell type 3 arises from Ly6C(+) monocyte-dendritic cell progenitors. Immunity 56, 1761–1777.e6. https://doi.org/10.1016/j.immuni.2023.07.001.

16. Chen, W., Jin, B., Cheng, C., Peng, H., Zhang, X., Tan, W., Tang, R., Lian, X., Diao, H., Luo, N., et al. (2024). Single-cell profiling reveals kidney CD163(+) dendritic cell participation in human lupus nephritis. Ann. Rheum. Dis. 83, 608–623. https://doi.org/10.1136/ard-2023-224788.

17. Cheng, S., Li, Z., Gao, R., Xing, B., Gao, Y., Yang, Y., Qin, S., Zhang, L., Ouyang, H., Du, P., et al. (2021). A pan-cancer single-cell transcriptional atlas of tumor infiltrating myeloid cells. Cell 184, 792–809.e23. https://doi.org/10.1016/j.cell.2021.01.010.

18. Mulder, K., Patel, A.A., Kong, W.T., Piot, C., Halitzki, E., Dunsmore, G., Khalilnezhad, S., Irac, S.E., Dubuisson, A., Chevrier, M., et al. (2021). Cross-tissue single-cell landscape of human monocytes and macrophages in health and disease. Immunity 54, 1883–1900.e5. https://doi.org/10.1016/j.immuni.2021.07.007.

19. Nakamizo, S., Dutertre, C.A., Khalilnezhad, A., Zhang, X.M., Lim, S., Lum, J., Koh, G., Foong, C., Yong, P.J.A., Tan, K.J., et al. (2021). Single-cell analysis of human skin identifies CD14+ type 3 dendritic cells co-producing IL1B and IL23A in psoriasis. J. Exp. Med. 218, e20202345. https://doi.org/10.1084/jem.20202345.

20. Hiddingh, S., Pandit, A., Verhagen, F., Rijken, R., Servaas, N.H., Wichers, R.C.G.K., Loon, N.H.T.D., Imhof, S.M., Radstake, T.R.D.J., de Boer, J.H., et al. (2023). Transcriptome network analysis implicates CX3CR1-positive type 3 dendritic cells in non-infectious uveitis. eLife 12, e74913. https://doi.org/10.7554/eLife.74913.

21. Maier, B., Leader, A.M., Chen, S.T., Tung, N., Chang, C., LeBerichel, J., Chudnovskiy, A., Maskey, S., Walker, L., Finnigan, J.P., et al. (2020). Author Correction: A conserved dendritic-cell regulatory program limits antitumour immunity. Nature 582, E17. https://doi.org/10.1038/s41586-020-2326-5.

22. Ginhoux, F., Guilliams, M., and Merad, M. (2022). Expanding dendritic cell nomenclature in the single-cell era. Nat. Rev. Immunol. 22, 67–68. https://doi.org/10.1038/s41577-022-00675-7.

23. Jongbloed, S.L., Lebre, M.C., Fraser, A.R., Gracie, J.A., Sturrock, R.D., Tak, P.P., and McInnes, I.B. (2006). Enumeration and phenotypical analysis of distinct dendritic cell subsets in psoriatic arthritis and rheumatoid arthritis. Arthritis Res. Ther. 8, R15. https://doi.org/10.1186/ar1864.

24. Lebre, M.C., Jongbloed, S.L., Tas, S.W., Smeets, T.J.M., McInnes, I.B., and Tak, P.P. (2008). Rheumatoid arthritis synovium contains two subsets of CD83-DC-LAMP- dendritic cells with distinct cytokine profiles. Am. J. Pathol. 172, 940–950. https://doi.org/10.2353/ajpath.2008.070703.

25. Moret, F.M., Hack, C.E., van der Wurff-Jacobs, K.M.G., de Jager, W., Radstake, T.R.D.J., Lafeber, F.P.J.G., and van Roon, J.A.G. (2013). Intra-articular CD1c-expressing myeloid dendritic cells from rheumatoid arthritis patients express a unique set of T cell-attracting chemokines and spontaneously induce Th1, Th17 and Th2 cell activity. Arthritis Res. Ther. 15, R155. https://doi.org/10.1186/ar4338.

26. Canavan, M., Marzaioli, V., Bhargava, V., Nagpal, S., Gallagher, P., Hurson, C., Mullan, R., Veale, D.J., and Fearon, U. (2021). Functionally mature CD1c(+) dendritic cells preferentially accumulate in the

inflammatory arthritis synovium. Front. Immunol. *12*, 745226. https://doi.org/10.3389/fimmu.2021.745226.

27. Canavan, M., Walsh, A.M., Bhargava, V., Wade, S.M., McGarry, T., Marzaioli, V., Moran, B., Biniecka, M., Convery, H., Wade, S., et al. (2018). Enriched CD141+ DCs in the joint are transcriptionally distinct, activated, and contribute to joint pathogenesis. JCI Insight *3*. https://doi.org/10.1172/jci.insight.95228.

28. Kurowska-Stolarska, M., Alivernini, S., Melchor, E.G., Elmesmari, A., Tolusso, B., Tange, C., Petricca, L., Gilchrist, D.S., Di Sante, G., Keijzer, C., et al. (2017). MicroRNA-34a dependent regulation of AXL controls the activation of dendritic cells in inflammatory arthritis. Nat. Commun. *8*, 15877. https://doi.org/10.1038/ncomms15877.

29. Cavanagh, L.L., Boyce, A., Smith, L., Padmanabha, J., Filgueira, L., Pietschmann, P., and Thomas, R. (2005). Rheumatoid arthritis synovium contains plasmacytoid dendritic cells. Arthritis Res. Ther. *7*, R230–R240. https://doi.org/10.1186/ar1467.

30. Alivernini, S., MacDonald, L., Elmesmari, A., Finlay, S., Tolusso, B., Gigante, M.R., Petricca, L., Di Mario, C., Bui, L., Perniola, S., et al. (2020). Distinct synovial tissue macrophage subsets regulate inflammation and remission in rheumatoid arthritis. Nat. Med. *26*, 1295–1306. https://doi.org/10.1038/s41591-020-0939-8.

31. Culemann, S., Grüneboom, A., Nicolás-Ávila, J.Á., Weidner, D., Lämmle, K.F., Rothe, T., Quintana, J.A., Kirchner, P., Krljanac, B., Eberhardt, M., et al. (2019). Locally renewing resident synovial macrophages provide a protective barrier for the joint. Nature *572*, 670–675. https://doi.org/10.1038/s41586-019-1471-1.

32. Chakarov, S., Lim, H.Y., Tan, L., Lim, S.Y., See, P., Lum, J., Zhang, X.M., Foo, S., Nakamizo, S., Duan, K., et al. (2019). Two distinct interstitial macrophage populations coexist across tissues in specific subtissular niches. Science *363*, eaau0964. https://doi.org/10.1126/science.aau0964.

33. Lubin, R., Patel, A.A., Mackerodt, J., Zhang, Y., Gvili, R., Mulder, K., Dutertre, C.A., Jalali, P., Glanville, J.R.W., Hazan, I., et al. (2024). The lifespan and kinetics of human dendritic cell subsets and their precursors in health and inflammation. J. Exp. Med. *221*, e20220867. https://doi.org/10.1084/jem.20220867.

34. Pang, X., He, X., Qiu, Z., Zhang, H., Xie, R., Liu, Z., Gu, Y., Zhao, N., Xiang, Q., and Cui, Y. (2023). Targeting integrin pathways: mechanisms and advances in therapy. Signal Transduct. Target. Ther. *8*, 1. https://doi.org/10.1038/s41392-022-01259-6.

35. Ahmat Amin, M.K.B., Shimizu, A., and Ogita, H. (2019). The pivotal roles of the epithelial membrane protein family in cancer invasiveness and metastasis. Cancers (Basel) *11*, 1620. https://doi.org/10.3390/cancers11111620.

36. Rothlin, C.V., and Lemke, G. (2010). TAM receptor signaling and autoimmune disease. Curr. Opin. Immunol. *22*, 740–746. https://doi.org/10.1016/j.coi.2010.10.001.

37. Carrera Silva, E.A., Chan, P.Y., Joannas, L., Errasti, A.E., Gagliani, N., Bosurgi, L., Jabbour, M., Perry, A., Smith-Chakmakova, F., Mucida, D., et al. (2013). T cell-derived protein S engages TAM receptor signaling in dendritic cells to control the magnitude of the immune response. Immunity *39*, 160–170. https://doi.org/10.1016/j.immuni.2013.06.010.

38. Singh, S.S., Chauhan, S.B., Kumar, A., Kumar, S., Engwerda, C.R., Sundar, S., and Kumar, R. (2022). Amphiregulin in cellular physiology, health, and disease: potential use as a biomarker and therapeutic target. J. Cell. Physiol. *237*, 1143–1156. https://doi.org/10.1002/jcp.30615.

39. Hu, Y., Recouvreux, M.S., Haro, M., Taylan, E., Taylor-Harding, B., Walts, A.E., Karlan, B.Y., and Orsulic, S. (2024). INHBA(+) cancer-associated fibroblasts generate an immunosuppressive tumor microenvironment in ovarian cancer. NPJ Precis. Oncol. *8*, 35. https://doi.org/10.1038/s41698-024-00523-y.

40. DeVito, N.C., Sturdivant, M., Thievanthiran, B., Xiao, C., Plebanek, M.P., Salama, A.K.S., Beasley, G.M., Holtzhausen, A., Novotny-Diermayr, V., Strickler, J.H., et al. (2021). Pharmacological Wnt ligand inhibition overcomes key tumor-mediated resistance pathways to anti-PD-1 immuno-

therapy. Cell Rep. *35*, 109071. https://doi.org/10.1016/j.celrep.2021.109071.

41. Clayton, S.A., Daley, K.K., MacDonald, L., Fernandez-Vizarra, E., Bottegoni, G., O'Neil, J.D., Major, T., Griffin, D., Zhuang, Q., Adewoye, A.B., et al. (2021). Inflammation causes remodeling of mitochondrial cytochrome c oxidase mediated by the bifunctional gene C15orf48. Sci. Adv. *7*, eabl5182. https://doi.org/10.1126/sciadv.abl5182.

42. Zhang, F., Jonsson, A.H., Nathan, A., Millard, N., Curtis, M., Xiao, Q., Gutierrez-Arcelus, M., Apruzzese, W., Watts, G.F.M., Weisenfeld, D., et al. (2023). Deconstruction of rheumatoid arthritis synovium defines inflammatory subtypes. Nature *623*, 616–624. https://doi.org/10.1038/s41586-023-06708-y.

43. Lang, R., and Raffi, F.A.M. (2019). Dual-specificity phosphatases in immunity and infection: an update. Int. J. Mol. Sci. *20*, 2710. https://doi.org/10.3390/ijms20112710.

44. Vogt, L., Schmitz, N., Kurrer, M.O., Bauer, M., Hinton, H.I., Behnke, S., Gatto, D., Sebbel, P., Beerli, R.R., Sonderegger, I., et al. (2006). VSIG4, a B7 family-related protein, is a negative regulator of T cell activation. J. Clin. Invest. *116*, 2817–2826. https://doi.org/10.1172/JCI25673.

45. Whitmore, M.M., Iparraguirre, A., Kubelka, L., Weninger, W., Hai, T., and Williams, B.R.G. (2007). Negative regulation of TLR-signaling pathways by activating transcription factor-3. J. Immunol. *179*, 3622–3630. https://doi.org/10.4049/jimmunol.179.6.3622.

46. Kurowska-Stolarska, M., Alivernini, S., Ballantine, L.E., Asquith, D.L., Millar, N.L., Gilchrist, D.S., Reilly, J., Ierna, M., Fraser, A.R., Stolarski, B., et al. (2011). MicroRNA-155 as a proinflammatory regulator in clinical and experimental arthritis. Proc. Natl. Acad. Sci. USA *108*, 11193–11198. https://doi.org/10.1073/pnas.1019536108.

47. Li, J., Zhou, J., Huang, H., Jiang, J., Zhang, T., and Ni, C. (2023). Mature dendritic cells enriched in immunoregulatory molecules (mregDCs): A novel population in the tumour microenvironment and immunotherapy target. Clin. Transl. Med. *13*, e1199. https://doi.org/10.1002/ctm2.1199.

48. Mayer, J.U., Brown, S.L., MacDonald, A.S., and Milling, S.W. (2020). Defined intestinal regions are drained by specific lymph nodes that mount distinct Th1 and Th2 responses against Schistosoma mansoni Eggs. Front. Immunol. *11*, 592325. https://doi.org/10.3389/fimmu.2020.592325.

49. Greenwald, N.F., Miller, G., Moen, E., Kong, A., Kagel, A., Dougherty, T., Fullaway, C.C., McIntosh, B.J., Leow, K.X., Schwartz, M.S., et al. (2022). Whole-cell segmentation of tissue images with human-level performance using large-scale data annotation and deep learning. Nat. Biotechnol. *40*, 555–565. https://doi.org/10.1038/s41587-021-01094-0.

50. Petukhov, V., Xu, R.J., Soldatov, R.A., Cadinu, P., Khodosevich, K., Moffitt, J.R., and Kharchenko, P.V. (2022). Cell segmentation in imaging-based spatial transcriptomics. Nat. Biotechnol. *40*, 345–354. https://doi.org/10.1038/s41587-021-01044-w.

51. Weyand, C.M., and Goronzy, J.J. (2003). Ectopic germinal center formation in rheumatoid synovitis. Ann. N. Y. Acad. Sci. *987*, 140–149. https://doi.org/10.1111/j.1749-6632.2003.tb06042.x.

52. Zhang, F., Wei, K., Slowikowski, K., Fonseka, C.Y., Rao, D.A., Kelly, S., Goodman, S.M., Tabechian, D., Hughes, L.B., Salomon-Escoto, K., et al. (2019). Defining inflammatory cell states in rheumatoid arthritis joint synovial tissues by integrating single-cell transcriptomics and mass cytometry. Nat. Immunol. *20*, 928–942. https://doi.org/10.1038/s41590-019-0378-1.

53. Rao, D.A., Gurish, M.F., Marshall, J.L., Slowikowski, K., Fonseka, C.Y., Liu, Y., Donlin, L.T., Henderson, L.A., Wei, K., Mizoguchi, F., et al. (2017). Pathologically expanded peripheral T helper cell subset drives B cells in rheumatoid arthritis. Nature *542*, 110–114. https://doi.org/10.1038/nature20810.

54. Magen, A., Hamon, P., Fiaschi, N., Soong, B.Y., Park, M.D., Mattiuz, R., Humblin, E., Troncoso, L., D'Souza, D., Dawson, T., et al. (2023). Intratumoral dendritic cell-CD4(+) T helper cell niches enable CD8(+) T cell differentiation following PD-1 blockade in hepatocellular carcinoma. Nat. Med. *29*, 1389–1399. https://doi.org/10.1038/s41591-023-02345-0.

55. Chang, M.H., Levescot, A., Nelson-Maney, N., Blaustein, R.B., Winden, K.D., Morris, A., Wactor, A., Balu, S., Grieshaber-Bouyer, R., Wei, K., et al. (2021). Arthritis flares mediated by tissue-resident memory T cells in the joint. Cell Rep. 37, 109902. https://doi.org/10.1016/j.celrep.2021.109902.

56. Mackay, F., and Browning, J.L. (2002). BAFF: a fundamental survival factor for B cells. Nat. Rev. Immunol. 2, 465–475. https://doi.org/10.1038/nri844.

57. Zheng, Y., Zhao, J., Shan, Y., Guo, S., Schrodi, S.J., and He, D. (2023). Role of the granzyme family in rheumatoid arthritis: current Insights and future perspectives. Front. Immunol. 14, 1137918. https://doi.org/10.3389/fimmu.2023.1137918.

58. Baker, K.F., Skelton, A.J., Lendrem, D.W., Scadeng, A., Thompson, B., Pratt, A.G., and Isaacs, J.D. (2019). Predicting drug-free remission in rheumatoid arthritis: A prospective interventional cohort study. J. Autoimmun. 105, 102298. https://doi.org/10.1016/j.jaut.2019.06.009.

59. Baker, K.F., McDonald, D., Hulme, G., Hussain, R., Coxhead, J., Swan, D., Schulz, A.R., Mei, H.E., MacDonald, L., Pratt, A.G., et al. (2024). Single-cell insights into immune dysregulation in rheumatoid arthritis flare versus drug-free remission. Nat. Commun. 15, 1063. https://doi.org/10.1038/s41467-024-45213-2.

60. Orange, D.E., Yao, V., Sawicka, K., Fak, J., Frank, M.O., Parveen, S., Blachere, N.E., Hale, C., Zhang, F., Raychaudhuri, S., et al. (2020). RNA identification of PRIME cells predicting rheumatoid arthritis flares. N. Engl. J. Med. 383, 218–228. https://doi.org/10.1056/NEJMoa2004114.

61. Cohen, M., Giladi, A., Barboy, O., Hamon, P., Li, B., Zada, M., Gurevich-Shapiro, A., Beccaria, C.G., David, E., Maier, B.B., et al. (2022). The interaction of CD4(+) helper T cells with dendritic cells shapes the tumor microenvironment and immune checkpoint blockade response. Nat. Cancer 3, 303–317. https://doi.org/10.1038/s43018-022-00338-5.

62. Kurowska-Stolarska, M., and Alivernini, S. (2022). Synovial tissue macrophages in joint homeostasis, rheumatoid arthritis and disease remission. Nat. Rev. Rheumatol. 18, 384–397. https://doi.org/10.1038/s41584-022-00790-8.

63. Pitzalis, C., Kelly, S., and Humby, F. (2013). New learnings on the pathophysiology of RA from synovial biopsies. Curr. Opin. Rheumatol. 25, 334–344. https://doi.org/10.1097/BOR.0b013e32835fd8eb.

64. James, E.A., Rieck, M., Pieper, J., Gebe, J.A., Yue, B.B., Tatum, M., Peda, M., Sandin, C., Klareskog, L., Malmström, V., et al. (2014). Citrulline-specific Th1 cells are increased in rheumatoid arthritis and their frequency is influenced by disease duration and therapy. Arthritis Rheumatol. 66, 1712–1722. https://doi.org/10.1002/art.38637.

65. Kästele, V., Mayer, J., Lee, E.S., Papazian, N., Cole, J.J., Cerovic, V., Belz, G., Tomura, M., Eberl, G., Goodyear, C., et al. (2021). Intestinal-derived ILCs migrating in lymph increase IFNgamma production in response to Salmonella Typhimurium infection. Mucosal Immunol. 14, 717–727. https://doi.org/10.1038/s41385-020-00366-3.

66. Stuart, T., Butler, A., Hoffman, P., Hafemeister, C., Papalexi, E., Mauck, W.M., 3rd, Hao, Y., Stoeckius, M., Smibert, P., and Satija, R. (2019). Comprehensive integration of single-cell data. Cell 177, 1888–1902.e21. https://doi.org/10.1016/j.cell.2019.05.031.

67. Young, M.D., and Behjati, S. (2020). SoupX removes ambient RNA contamination from droplet-based single-cell RNA sequencing data. GigaScience 9, giaa151. https://doi.org/10.1093/gigascience/giaa151.

68. McGinnis, C.S., Murrow, L.M., and Gartner, Z.J. (2019). DoubletFinder: doublet detection in single-cell RNA sequencing data using artificial nearest neighbors. Cell Syst. 8, 329–337.e4. https://doi.org/10.1016/j.cels.2019.03.003.

69. Boggy, G.J., McElfresh, G.W., Mahyari, E., Ventura, A.B., Hansen, S.G., Picker, L.J., and Bimber, B.N. (2022). BFF and cellhashR: analysis tools for accurate demultiplexing of cell hashing data. Bioinformatics 38, 2791–2801. https://doi.org/10.1093/bioinformatics/btac213.

70. Heaton, H., Talman, A.M., Knights, A., Imaz, M., Gaffney, D.J., Durbin, R., Hemberg, M., and Lawniczak, M.K.N. (2020). Souporcell: robust clustering of single-cell RNA-seq data by genotype without reference genotypes. Nat. Methods 17, 615–620. https://doi.org/10.1038/s41592-020-0820-1.

71. Korsunsky, I., Millard, N., Fan, J., Slowikowski, K., Zhang, F., Wei, K., Baglaenko, Y., Brenner, M., Loh, P.R., and Raychaudhuri, S. (2019). Fast, sensitive and accurate integration of single-cell data with Harmony. Nat. Methods 16, 1289–1296. https://doi.org/10.1038/s41592-019-0619-0.

72. Schubert, M., Klinger, B., Klünemann, M., Sieber, A., Uhlitz, F., Sauer, S., Garnett, M.J., Blüthgen, N., and Saez-Rodriguez, J. (2018). Perturbation-response genes reveal signaling footprints in cancer gene expression. Nat. Commun. 9, 20. https://doi.org/10.1038/s41467-017-02391-6.

73. La Manno, G., Soldatov, R., Zeisel, A., Braun, E., Hochgerner, H., Petukhov, V., Lidschreiber, K., Kastriti, M.E., Lönnerberg, P., Furlan, A., et al. (2018). RNA velocity of single cells. Nature 560, 494–498. https://doi.org/10.1038/s41586-018-0414-6.

74. Wolf, F.A., Angerer, P., and Theis, F.J. (2018). SCANPY: large-scale single-cell gene expression data analysis. Genome Biol. 19, 15. https://doi.org/10.1186/s13059-017-1382-0.

75. Bergen, V., Lange, M., Peidli, S., Wolf, F.A., and Theis, F.J. (2020). Generalizing RNA velocity to transient cell states through dynamical modeling. Nat. Biotechnol. 38, 1408–1414. https://doi.org/10.1038/s41587-020-0591-3.

76. Wolf, F.A., Hamey, F.K., Plass, M., Solana, J., Dahlin, J.S., Göttgens, B., Rajewsky, N., Simon, L., and Theis, F.J. (2019). PAGA: graph abstraction reconciles clustering with trajectory inference through a topology preserving map of single cells. Genome Biol. 20, 59. https://doi.org/10.1186/s13059-019-1663-x.

77. Troulé, K., Petryszak, R., Prete, M., Cranley, J., Harasty, A., Kelvin Tuong, Z., Teichmann, S.A., Garcia-Alonso, L., and Vento-Tormo, R. (2023). CellPhoneDB v5: Inferring Cell-Cell Communication from Single-Cell Multiomics Data. Preprint at arXiv. https://doi.org/10.48550/arXiv.2311.04567.

78. Love, M.I., Huber, W., and Anders, S. (2014). Moderated estimation of fold change and dispersion for RNA-seq data with DESeq2. Genome Biol. 15, 550. https://doi.org/10.1186/s13059-014-0550-8.

79. Ritchie, M.E., Phipson, B., Wu, D., Hu, Y., Law, C.W., Shi, W., and Smyth, G.K. (2015). limma powers differential expression analyses for RNA-sequencing and microarray studies. Nucleic Acids Res. 43, e47. https://doi.org/10.1093/nar/gkv007.

80. Leek, J.T., Johnson, W.E., Parker, H.S., Jaffe, A.E., and Storey, J.D. (2012). The sva package for removing batch effects and other unwanted variation in high-throughput experiments. Bioinformatics 28, 882–883. https://doi.org/10.1093/bioinformatics/bts034.

81. Hänzelmann, S., Castelo, R., and Guinney, J. (2013). GSVA: gene set variation analysis for microarray and RNA-seq data. BMC Bioinformatics 14, 7. https://doi.org/10.1186/1471-2105-14-7.

82. Alquicira-Hernandez, J., and Powell, J.E. (2021). Nebulosa recovers single-cell gene expression signals by kernel density estimation. Bioinformatics 37, 2485–2487. https://doi.org/10.1093/bioinformatics/btab003.

83. Dobin, A., Davis, C.A., Schlesinger, F., Drenkow, J., Zaleski, C., Jha, S., Batut, P., Chaisson, M., and Gingeras, T.R. (2013). STAR: ultrafast universal RNA-seq aligner. Bioinformatics 29, 15–21. https://doi.org/10.1093/bioinformatics/bts635.

84. Aletaha, D., Neogi, T., Silman, A.J., Funovits, J., Felson, D.T., Bingham, C.O., 3rd, Birnbaum, N.S., Burmester, G.R., Bykerk, V.P., Cohen, M.D., et al. (2010). 2010 rheumatoid arthritis classification criteria: an American College of Rheumatology/European League Against Rheumatism collaborative initiative. Ann. Rheum. Dis. 69, 1580–1588. https://doi.org/10.1136/ard.2010.138461.

85. Alivernini, S., Tolusso, B., Gessi, M., Gigante, M.R., Mannocci, A., Petricca, L., Perniola, S., Di Mario, C., Bui, L., Fedele, A.L., et al. (2021). Inclusion of synovial tissue-derived characteristics in a nomogram for the prediction of treatment response in treatment-naive rheumatoid arthritis patients. Arthritis Rheumatol. 73, 1601–1613. https://doi.org/10.1002/art.41726.

86. Alivernini, S., Tolusso, B., Petricca, L., Bui, L., Di Sante, G., Peluso, G., Benvenuto, R., Fedele, A.L., Federico, F., Ferraccioli, G., et al. (2017). Synovial features of patients with rheumatoid arthritis and psoriatic arthritis in clinical and ultrasound remission differ under anti-TNF therapy: a clue to interpret different chances of relapse after clinical remission? Ann. Rheum. Dis. *76*, 1228–1236. https://doi.org/10.1136/annrheumdis-2016-210424.

87. Nagy, G., Roodenrijs, N.M.T., Welsing, P.M., Kedves, M., Hamar, A., van der Goes, M.C., Kent, A., Bakkers, M., Blaas, E., Senolt, L., et al. (2021). EULAR definition of difficult-to-treat rheumatoid arthritis. Ann. Rheum. Dis. *80*, 31–35. https://doi.org/10.1136/annrheumdis-2020-217344.

88. Alivernini, S., Peluso, G., Fedele, A.L., Tolusso, B., Gremese, E., and Ferraccioli, G. (2016). Tapering and discontinuation of TNF-alpha blockers without disease relapse using ultrasonography as a tool to identify patients with rheumatoid arthritis in clinical and histological remission. Arthritis Res. Ther. *18*, 39. https://doi.org/10.1186/s13075-016-0927-z.

89. Arnett, F.C., Edworthy, S.M., Bloch, D.A., McShane, D.J., Fries, J.F., Cooper, N.S., Healey, L.A., Kaplan, S.R., Liang, M.H., and Luthra, H.S. (1988). The American Rheumatism Association 1987 revised criteria for the classification of rheumatoid arthritis. Arthritis Rheum. *31*, 315–324. https://doi.org/10.1002/art.1780310302.

90. van de Sande, M.G.H., Gerlag, D.M., Lodde, B.M., van Baarsen, L.G.M., Alivernini, S., Codullo, V., Felea, I., Vieira-Sousa, E., Fearon, U., Reece, R., et al. (2011). Evaluating antirheumatic treatments using synovial bi-opsy: a recommendation for standardisation to be used in clinical trials. Ann. Rheum. Dis. *70*, 423–427. https://doi.org/10.1136/ard.2010.139550.

91. Germain, P.L., Sonrel, A., and Robinson, M.D. (2020). pipeComp, a general framework for the evaluation of computational pipelines, reveals performant single cell RNA-seq preprocessing tools. Genome Biol. *21*, 227. https://doi.org/10.1186/s13059-020-02136-7.

92. Moreau, M.X., Saillour, Y., Cwetsch, A.W., Pierani, A., and Causeret, F. (2021). Single-cell transcriptomics of the early developing mouse cerebral cortex disentangle the spatial and temporal components of neuronal fate acquisition. Development *148*, dev197962. https://doi.org/10.1242/dev.197962.

93. Chen, J.H., Nieman, L.T., Spurrell, M., Jorgji, V., Elmelech, L., Richieri, P., Xu, K.H., Madhu, R., Parikh, M., Zamora, I., et al. (2024). Human lung cancer harbors spatially organized stem-immunity hubs associated with response to immunotherapy. Nat. Immunol. *25*, 644–658. https://doi.org/10.1038/s41590-024-01792-2.

94. McInnes, L., Healy, J., Saul, N., and Großberger, L. (2018). UMAP: uniform manifold approximation and projection. J. Open Source Software *3*, 861. https://doi.org/10.21105/joss.00861.

95. Mayer, J.U., Demiri, M., Agace, W.W., MacDonald, A.S., Svensson-Frej, M., and Milling, S.W. (2017). Different populations of CD11b(+) dendritic cells drive Th2 responses in the small intestine and colon. Nat. Commun. *8*, 15820. https://doi.org/10.1038/ncomms15820.

STAR★METHODS

KEY RESOURCES TABLE

REAGENT or RESOURCE	SOURCE	IDENTIFIER
Antibodies		
PE/Dazzle594 anti-human CD45	BioLegend	Cat#304052, RRID:AB_2563568
Brilliant Violet 605 anti-human CD45	BioLegend	Cat#304041, RRID:AB_2562105
Brilliant Violet 711 anti-human CD45	BioLegend	Cat#304050, RRID:AB_2563466
AF700 anti-human anti-human HLA-DR	BioLegend	Cat#307626, RRID:AB_493771
Brilliant Violet 785 anti-human HLA-DR	BioLegend	Cat#307642, RRID:AB_2563461
APC anti-human MERTK	BioLegend	Cat#367612, RRID:AB_2687289
APC anti-human Folate Receptor b	BioLegend	Cat#391706, RRID:AB_2721303
PE anti-human CD301 (CLEC10A)	BioLegend	Cat#354704,RRID:AB_11219002
Brilliant Violet 421 anti-human CD1c	BioLegend	Cat#331525,RRID:AB_10933249
Brilliant Violet 510 anti-human CD1c	BioLegend	Cat#331534, RRID:AB_2566119
Brilliant Violet 510 anti-human CD14	BioLegend	Cat#301841, RRID:AB_2561946
Brilliant Violet 650 anti-human CD14	BioLegend	Cat#301830, RRID:AB_10959324
PE/CY7 anti-human CD11c	BioLegend	Cat#337216, RRID:AB_2129790
PE/CY7 anti-human CD9	BioLegend	Cat#312116, RRID:AB_2728256
PerCP_Cy5.5_anti-human CD32	BioLegend	Cat#303216, RRID:AB_2616925
PerCP_Cy5.5_anti-human CD39	BioLegend	Cat#328218, RRID:AB_2562897
FITC anti-human CD15 (SSEA-1)	BioLegend	Cat#323004, RRID:AB_756010
AF700 anti-human CD15 (SSEA-1)	BioLegend	Cat#323026, RRID:AB_2561427
FITC anti-human CD19	BioLegend	Cat#302206, RRID:AB_314236
AF700 anti-human CD19	BioLegend	Cat#302226, RRID:AB_493751
FITC anti-human CD20	BioLegend	Cat#302304, RRID:AB_314252
AF700 anti-human CD20	BioLegend	Cat#302322, RRID:AB_493753
FITC anti-human CD117 (c-kit)	BioLegend	Cat#313232, RRID:AB_2566219
AF700 anti-human CD117 (c-kit)	BioLegend	Cat#313246, RRID:AB_2860834
FITC anti-human CD56 (NCAM)-	BioLegend	Cat#304604, RRID:AB_314446
AF700 anti-human CD56 (NCAM)-	BioLegend	Cat#362522, RRID:AB_2564099
FITC anti-human CD3	BioLegend	Cat#300440, RRID:AB_2562046
AF700 anti-human CD3	BioLegend	Cat#300424, RRID:AB_493741
Brilliant Violet 711 anti-human CD45	BioLegend	Cat#304050, RRID:AB_2563466
PE/CY7 anti-human CD4	BioLegend	Cat#300512, RRID:AB_314080
APC anti-human CD45RO	BioLegend	Cat#304210, RRID:AB_314426
FITC anti-human CD69	BioLegend	Cat#310904, RRID:AB_314838
Brilliant Violet 650 anti-human PD-1	BioLegend	Cat#329950, RRID:AB_2566362
Brilliant Violet 605 anti-human CXCR5	BioLegend	Cat#356930, RRID:AB_2566227
PE/CY7 anti-human IL-10	BioLegend	Cat#501420, RRID:AB_2125385
PE/Dazzle594 anti-human FOXP3	BioLegend	Cat#320126, RRID:AB_2564025
APC anti-human BAFF	BioLegend	Cat#366508, RRID:AB_2565711
AF700 anti-human IFN-γ	BioLegend	Cat#502520, RRID:AB_528921
PerCP_Cy5.5_anti-human CCL5	BioLegend	Cat#515508, RRID:AB_2562666
PE anti-human CXCL13	R&D system	Cat#IC8012P
BUV395 anti-human CD8	BD Bioscience	Cat#563795, RRID:AB_2722501
BUV737 anti-human CD19	BD Bioscience	Cat#741829, RRID:AB_2871164
Brilliant Violet 421 anti-human PD-1	BD Bioscience	Cat#564323, RRID:AB_2738745
Brilliant Violet 510 anti-human CD3	BioLegend	Cat#300448, RRID:AB_2563468

(Continued on next page)

Continued

REAGENT or RESOURCE	SOURCE	IDENTIFIER
PE/CY7 anti-human CD45RO	BioLegend	Cat#304230, RRID:AB_11203900
AF700 anti-human CD4	BioLegend	Cat#344622, RRID:AB_2563150
PerCP_Cy5.5_anti-human CD15	BioLegend	Cat#323020, RRID:AB_893257
PerCP_Cy5.5_anti-human CD66b	BioLegend	Cat#305108, RRID:AB_2077855
PerCP_Cy5.5_anti-human CD203c	BioLegend	Cat#324608, RRID:AB_2099775
anti-mouse CD16/32	BioLegend	Cat#101320, RRID:AB_1574975
Brilliant Violet 785 anti-mouse I-A/I-E	BioLegend	Cat#107645, RRID:AB_2565977
Brilliant Violet 711 anti-mouse CD8a	BioLegend	Cat#100759, RRID:AB_2563510
Brilliant Violet 650 anti-mouse CD127 (IL-7Rα)	BioLegend	Cat#135043, RRID:AB_2629681
Brilliant Violet 605 anti-mouse/human CD11b	BioLegend	Cat#101257, RRID:AB_2565431
Brilliant Violet 510 anti-mouse CD103	BioLegend	Cat#121423, RRID:AB_2562713
Brilliant Violet 421 anti-mouse CD206 (MMR)	BioLegend	Cat#141717, RRID:AB_2562232
PerCP/Cyanine5.5 anti-mouse CD64 (FcγRI)	BioLegend	Cat#139308, RRID:AB_2561963
FITC anti-mouse CD45	BioLegend	Cat#103108, RRID:AB_312973
Alexa Fluor® 700 anti-mouse Ly-6C	BioLegend	Cat#128024, RRID:AB_10643270
PE/Cyanine7 anti-mouse CD40	BioLegend	Cat#124622, RRID:AB_10897812
PE/Cyanine5 anti-mouse CD11c	BioLegend	Cat#117316, RRID:AB_493566
PE/Dazzle™ 594 anti-mouse CD197 (CCR7)	BioLegend	Cat#120122, RRID:AB_2564317
PE anti-mouse CD19	BioLegend	Cat#115508, RRID:AB_313643
PE anti-mouse CD3ε	BioLegend	Cat#100308, RRID:AB_312673
PE anti-mouse Ly-6G	BioLegend	Cat#127608, RRID:AB_1186099
PE anti-mouse NK-1.1	BioLegend	Cat#108708, RRID:AB_313395
Rabbit anti-human CLEC10A	Abcam plc	Cat#Ab197346
Rabbit anti-human AXL	Abcam plc	Cat#Ab219651
Mouse anti-human CD1c	Abcam plc	Cat#Ab156708,RRID:AB_2889187
Rabbit anti-human LAMP3	ThermoFisher	Cat# PA5-84069, RRID:AB_2791221
Mouse anti-human CD68	Dako	Cat#M087629-2
Goat anti-Rabbit IgG Alexa Fluor 488	ThermoFisher	Cat#A-11008, RRID:AB_143165
Goat anti-Rabbit IgG Alexa Fluor 660	ThermoFisher	Cat#A-21074, RRID:AB_2535735
Goat anti-Mouse IgG Alexa Fluor 660	ThermoFisher	Cat#A-21055, RRID:AB_1500636
Donkey anti-Mouse IgG Alexa Fluor 448	ThermoFisher	Cat#A-21202, RRID:AB_141607
TotalSeqA-Human Universal Cocktail, V1.0	BioLegend	Cat#399907, RRID:AB_2888692
TotalSeq™-A0251 anti-human Hashtag 1	BioLegend	Cat# 394601, RRID:AB_2750015
TotalSeq™-A0252 anti-human Hashtag 2	BioLegend	Cat# 394603, RRID:AB_2750016
TotalSeq™-A0253 anti-human Hashtag 3	BioLegend	Cat# 394605, RRID:AB_2750017
TotalSeq™-A0254 anti-human Hashtag 4	BioLegend	Cat# 394607, RRID:AB_2750018
TotalSeq™-A0255 anti-human Hashtag 5	BioLegend	Cat# 394609, RRID:AB_2750019
TotalSeq™-A0256 anti-human Hashtag 6	BioLegend	Cat# 394611, RRID:AB_2750020
Purified anti-human CD3	BioLegend	Cat# 300401
Biological samples		
Ultrasound-guided RA synovial biopsy & RA peripheral blood	SYNGem, Fondazione Policlinico Universitario A. Gemelli IRCCS	28485/18, 30973/19 and 14996/20
Normal synovium attending arthroscopy for meniscal tear or cruciate ligament damage	NHS Greater Glasgow & Clyde	West of Scotland Research Ethics Committee (19/WS/0111)
Healthy donor peripheral blood	University of Glasgow	West of Scotland Research Ethics Committee (19/WS/0111)
Peripheral blood RA remission patients	BIORRA, University of Newcastle	National Health Service Health Research Authority (14/NE/1042)

Continued

REAGENT or RESOURCE	SOURCE	IDENTIFIER
Chemicals, peptides, and recombinant proteins		
Human serum	Sigma	Cat# H3667-20ML
X-VIVO 15 Serum-free Cell Medium	Lonza	Cat# LZBE02-060F
Human IL-15 Recombinant Protein	PeproTech	Cat# 200-15
Fixable Viability Dye eFluor 780	eBiosciences	Cat# 65-0865-14
Liberase™ TM Research Grade	Roche	Cat# 5401127001R
Accutase	BioLegend	Cat# 423201
CryoStor CS10	StemCel Stem cell technologies	Cat# 100-1061
Bambanker	Nippon Genetics	Cat# BB02
RPMI 1640 Medium	Gibco	Cat# 11875093
eBioscience™ Foxp3 / Transcription Factor Staining Buffer Set	eBioscience	Cat# 00-5523-00
Histopaque®-1077	Sigma-Aldrich	Cat# 10771
Penicillin-Streptomycin (10,000 U/mL)	Gibco	Cat# 15140122
eBioscience™ Cell Stimulation Cocktail (plus protein transport inhibitors) (500X)	eBioscience	Cat# 00-4975-93
Fetal Bovine Serum	Sigma-Aldrich	Cat# F9665
L-Glutamine	Sigma-Aldrich	Cat# G7513
DPBS 1X W-OUT Calcium	ThermoFisher	Cat# 14190094
Ethylenediaminetetraacetic acid disodium salt solution	Sigma-Aldrich	Cat# E7889
LPS	Sigma-Aldrich	Cat# L6529
Collagenase-D	Roche	Cat# 11088866001
Heparin sodium	Wockhardt UK	Cat# FP1079
Critical commercial assays		
Chromium Next GEM Single Cell 3' GEM, Library & Gel Bead Kit v3.1	10X Genomics	Cat# PN-1000121
Chromium Next GEM Chip G Single Cell Kit	10X Genomics	Cat# PN-1000120
Single Index Kit T Set A	10X Genomics	Cat# PN-1000213
BD Rhapsody Cartridge Reagent Kit	BD Bioscience	Cat# 633731
BD Rhapsody cDNA Kit	BD Bioscience	Cat# 633773
BD Tag library preparation kit	BD Bioscience	Cat# 633774
BD Rhapsody Immune Response Panel	BD Bioscience	Cat# 633750
BD Rhapsody WTA	BD Bioscience	Cat# 633801
BD Human Single-Cell Sample Multiplexing Kit	BD Bioscience	Cat# 633781
SORT-seq	Single cell discoveries	N/A
EasySep™ Human Memory CD4+ T Cell Enrichment Kit	Stem cell technologies	Cat# 19157
miRNeasy Micro Kit	Qiagen	Cat# 217084
miScript SybR Green PCR kit	Qiagen	Cat# 1046470
miScript Reverse transcription kit II	Qiagen	Cat# 218161
miScript pre-AMP PCR kit	Qiagen	Cat# 331451
Deposited data		
scRNAseq/CITEseq of healthy, RA and remission RA synovial tissue	This paper	Array Express E-MTAB-14213
Spatial transcriptomics of active RA and remission RA synovial tissue	This paper	BioStudies S-BSST1483
SORT-seq data of synovial tissue myeloid DC	This paper	Array Express E-MTAB-14198
ScRNAseq of paired peripheral blood and synovial tissue	This paper	Array Express E-MTAB-14192

Continued

REAGENT or RESOURCE	SOURCE	IDENTIFIER
scRNAseq of ST-DC and autologous CD4 memory T cell coculture	This paper	Array Express E-MTAB-14191
scRNAseq of remission RA BioRRA cohort	This paper	Array Express E-MTAB-14169
SMARTseq2 single cell transcriptome data of human blood and tissue MNP	Mulder et al.[18]	GEO GSE178209
scRNAseq of healthy, active RA and remission RA synovial tissue	Alivernini et al.[30]	Array Express E-MTAB-8322
PRIME cell bulk RNA seq blood RA flare data	Orange et al.[60]	10.1056/NEJMoa2004114
Bulk RNA seq of murine CD11bposCD103pos myeloid DC2	Kästele et al.[65]	GEO GSE160156
Validation of ST-DC Cluster Markers in independent ST scRNAseq dataset	Zhang et al.[42]	https://doi.org/10.1038/s41586-023-06708-y
IF staining raw data	This paper	Bioimage Archive S-BIAD1388
Experimental models: Organisms/strains		
C57BL/6J (WT)	Jackson laboratories	Strain #:000664
B6.Cg-Mir155tm1Rsky/J (miR-155 deficient)	Jackson laboratories	Strain #:007745
Oligonucleotides		
10x Genomics SI-PCR primer: 5'AATGATACG GCGACCACCGAGATCTACACTCTTTCCCTACA CGACGC*T*C; * indicates a phosphorothioate bond	Eurofins Genomics	N/A
ADT cDNA PCR additive primer: 5'CCTTGGCACCCGAGAATT*C*C; * indicates a phosphorothioate bond	Eurofins Genomics	N/A
HTO cDNA PCR additive primer v2: 5'GTGACTGGAGTTCAGACGTGTGCTCTTCC GAT*C*T; * indicates a phosphorothioate bond	Eurofins Genomics	N/A
Illumina Small RNA RPI1 primer: 5'CAAGCAGAAGACGGCATACGAGATCGT GATGTGACTGGAGTTCCTTGGCACCCGAGA ATTC*C*A; * indicates a phosphorothioate bond	Eurofins Genomics	N/A
Illumina TruSeq D701_LONG primer: 5'CAAGCAGAAGACGGCATACGAGATCGAG TAATGTGACTGGAGTTCAGACGTGTGCTCTTC CGAT*C*T; * indicates a phosphorothioate bond	Eurofins Genomics	N/A
MIMAT0000646/hsa-miR-155-5p	Qiagen	Cat# MS00031486
Hs_RNU6-2_11	Qiagen	Cat# MS00033740
Dharmafect 3 transfection system	Dharmacon	Cat# T-2003-02
hsa-miR-155 mimic	Dharmacon	Cat# C300647-05-305
negative control miRNA mimic	Dharmacon	Cat# CN-001000-01-05
negative control labelled with 20nM Dy547 fluorochrome	Dharmacon	Cat# CP-004500-01-05
Software and algorithms		
FlowJo (10.8.2)	BD Bioscience	https://www.flowjo.com/
Cell Ranger (7.0.0)	10x Genomics	https://www.10xgenomics.com/products/chromium-analysis#cell-ranger
BD Genomics Rhapsody Analysis CWL (1.9.1)	SevenBridges	https://www.sevenbridges.com/
Seurat (4.0.3)	Stuart et al.[66]	https://satijalab.org/seurat/
SoupX (1.6.2)	Young and Behjati[67]	https://github.com/constantAmateur/SoupX
DoubletFinder (2.0.3)	McGinnis et al.[68]	https://github.com/chris-mcginnis-ucsf/DoubletFinder
cellhashR (1.0.3)	Boggy et al.[69]	https://github.com/BimberLab/cellhashR

(Continued on next page)

Continued

REAGENT or RESOURCE	SOURCE	IDENTIFIER
Souporcell (2.5)	Heaton et al.[70]	https://github.com/wheaton5/souporcell
SeuratWrappers (0.3.0)	Seurat	https://github.com/satijalab/seurat-wrappers/
Harmony (1.2.0)	Korsunsky et al.[71]	https://github.com/immunogenomics/harmony
PROGENy (1.24.0)	Schubert et al.[72]	https://github.com/saezlab/progeny
pheatmap (1.0.12)	https://github.com/raivokolde/pheatmap	N/A
Velocyto (0.17)	La Manno et al.[73]	https://github.com/velocyto-team/velocyto.py
SeuratDisk (0.0.0.9019)	https://github.com/mojaveazure/seurat-disk	N/A
scanpy (1.9.3)	Wolf et al.[74]	https://github.com/scverse/scanpy
scvelo (0.3.1)	Bergen et al.[75]	https://github.com/theislab/scvelo
AnnData (0.9.1)	https://github.com/scverse/anndata	N/A
PAGA (1.3.3)	Wolf et al.[76]	https://github.com/theislab/paga
CellphoneDB (5.0)	Troulé et al.[77]	https://github.com/ventolab/CellphoneDB
Python (3.8)	Python Software Foundation	https://www.python.org/
R (4.2.2)	The R Foundation	https://www.r-project.org/
ktplots (2.3.0)	Troulé et al.[77]	https://github.com/zktuong/ktplots
Mesmer (DeepCell)	Greenwald et al.[49]	https://github.com/vanvalenlab/deepcell-tf/blob/master/notebooks/applications/Mesmer-Application.ipynb
Baysor (0.6.2)	Petukhov et al.[50]	https://github.com/kharchenkolab/Baysor
uwot (0.1.16)	https://github.com/jlmelville/uwot/releases	N/A
presto (1.0.0)	Korsunsky et al.[71]	https://github.com/immunogenomics/presto/tree/glmm/
ggplot2 (2_3.4.4)	https://github.com/tidyverse/ggplot2	N/A
sf (1.0.16)	https://github.com/r-spatial/sf	N/A
DESeq2 (1.40.2)	Love et al.[78]	https://github.com/thelovelab/DESeq2
PCAtools (2.12.0)	https://github.com/kevinblighe/PCAtools	N/A
limma (3.56.2)	Ritchie et al.[79]	https://bioconductor.org/packages/release/bioc/html/limma.html
SVA (3.48.0)	Leek et al.[80]	https://github.com/jtleek/sva
lme4 (1.1-34)	https://github.com/lme4/lme4	N/A
GSVA (1.48.3)	Hänzelmann et al.[81]	https://github.com/rcastelo/GSVA
Nebulosa (0.99.92)	Alquicira-Hernandez et al.[82]	https://github.com/powellgenomicslab/Nebulosa
GraphPad Prism (10)	GraphPad	https://www.graphpad.com
STAR (2.7.11a)	Dobin et al.[83]	https://github.com/alexdobin/STAR
Bulk and single cell RNA-seq Analysis Scripts	This Paper	https://doi.org/10.5281/zenodo.13866418
Spatial Transcriptomic Data Analysis Scripts	This Paper	https://doi.org/10.5281/zenodo.13869471

(Continued on next page)

Continued		
REAGENT or RESOURCE	SOURCE	IDENTIFIER
Other		
14G Precisa Needle / Tru-cut semiautomatic device for histological biopsy	HS Hospital Service Italy	Cat#PRE1410
IgM-Rheumatoid Factor ELISA Assay	Orgentec Diagnostika, Bouty-UK	Cat# ORG522M
IgA- Rheumatoid Factor ELISA Assay	Orgentec Diagnostika, Bouty-UK	Cat# ORG522A
CCP ZENIT RA	Menarini Dagnostics, Italy	Cat# 41430

EXPERIMENTAL MODEL AND STUDY PARTICIPANTS

Human participants

Patients recruitment and management

To study ST-DCs and their interactions with T cells, 86 patients fulfilling the EULAR classification criteria revised criteria for RA[84] were enrolled and underwent ultrasound-guided ST biopsy of the knee or the wrist as a part of ongoing recruitment to the SYNGem cohort[30,85,86] (Division of Rheumatology, Fondazione Policlinico Universitario A. Gemelli IRCCS – Università Cattolica del Sacro Cuore, Rome). RA patients were stratified into treatment-naïve, treatment-resistant RA (inadequate responders to conventional or biological Disease Modifying Anti-Rheumatic Drugs, c/b DMARDs), difficult-to-treat RA (inadequate responders to two or more bDMARDs)[87] and patients in sustained (>9 months) clinical and ultrasound steroid-free remission maintained by stable conventional and/or biologic-DMARDs.[86] Healthy donors (n=12) attending arthroscopy for meniscal tear or cruciate ligament damage, with normal synovium (macroscopically and by MRI) were included as a control group (University of Glasgow). The criteria for RA patients in sustained clinical remission included (i) DAS44 (disease activity score in 44 joints)<1.6 or DAS28<2.6 at 3 sequential assessments (each 3 months apart), and (ii) ultrasound remission (Power Doppler negativity by US assessment at 3 sequential evaluations, each 3 months apart).[30,86,88] The clinical and laboratory evaluation of each RA patient enrolled included DAS based on the number of tender and swollen joints of 44 or 26 examined, plus the erythrocyte sedimentation rate (ESR) and plasma C-reactive protein (CRP). Peripheral blood samples were tested for IgA-RF and IgM-RF (Orgentec Diagnostika, Bouty-UK), and ACPA (Menarini Diagnostics-Italy) using commercial Enzyme-Linked Immunosorbent Assay (ELISA) and ChemiLuminescence Immunoassay (CLIA) respectively. Peripheral blood from additional 12 healthy donors matched by age and sex to the RA patients was collected.

To study the peripheral blood predecessors of ST dendritic cell clusters we used the BioRRA RA disease remission cohort.[58,59] Patients fulfilling the American College of Rheumatology (ACR) / European Alliance of Associations for Rheumatology (EULAR) 2010 or ACR 1987 classification criteria for RA[84,89] and in remission (DAS28-CRP< 2.4 and no Power Doppler signal on a 7-joint ultrasound examination) on cDMARDs (methotrexate, sulfasalazine and/or hydroxychloroquine therapy) stopped all DMARD therapy without tapering. Other medications, including non-steroidal anti-inflammatory drugs were continued if required. Study reviews were scheduled at months 1, 3 and 6, with additional study visits if requested by the patient. During each review, the maintenance of remission or the emergence of disease flare (defined as DAS28-CRP $\geq$ 2.4) was recorded.

The study protocols were approved by the Ethics Committee of the Università Cattolica del Sacro Cuore (28485/18, 30973/19 and 14996/20 for the SYNGem cohort), by the Northeast Tyne & Wear South Research Ethics Committee (National Health Service Health Research Authority, reference 14/NE/1042 for the BioRRA cohort) and by the West of Scotland Research Ethics Committee (19/WS/0111 for healthy donors). Use of BioRRA samples was authorised by the Newcastle Biobank Committee under the approval of the Northeast – Newcastle & North Tyneside 1 Research Ethics Committee (17/NE/0361). All subjects provided signed informed consent.

The exact number of patients constituting different data set and patients' demographic, and clinical information are provided in Table S1.

Animals

C57BL/6J (WT) and Cg-Mir155tm1Rsky/J were purchased from Jackson laboratories) and bred and maintained in groups of 1-5 animals per cage. Males aged 8 to 12 weeks were used for experimentation, as described in the method details section, in accordance with the approved protocols by the UK Home Office animal licenses.

METHOD DETAILS

Semiquantitative histological assessment of synovitis degree

Synovial tissue specimens were fixed in 10% neutral-buffered formalin and embedded in paraffin. Briefly, paraffin-embedded ST specimens were sectioned at 3μm. Sections were stained for Haematoxylin and Eosin as follows: sections were deparaffinized in xylene and rehydrated in a series of graded ethanol, stained in haematoxylin and counterstained in Eosin/Phloxine. Finally, sections were dehydrated, cleared in xylene and mounted with Bio Mount (Bio-Optica). Slides were examined using a light microscope (Leica

DM 2000). The severity of synovitis was graded according to the three synovial membrane features (synovial lining cell layer, stromal cell density and inflammatory infiltrate), each ranked on a scale from none (0), slight (1), moderate (2), and strong (3). The values of the parameters were summed and interpreted as follows: 0–1 no synovitis, 2–4 low-grade synovitis, and 5–9 high-grade synovitis.[85]

Sample preparation for single cell RNAseq and CITEseq of peripheral blood and ST

To investigate ST myeloid DC and T cell heterogeneity in RA, we sequenced the transcriptomic profile of 143,851 cells from peripheral blood mononuclear cells (PBMC) (n=8, including 3 matched with STs) and ST (ST) biopsies (n=34). The latter includes ST from healthy donors (n=7), patients with active RA (n=18) and patients in sustained remission (n=9). Synovial biopsies were taken using 14G Precisa Needle (HS Hospital Service, Italy) in ultrasound-guided protocol,[30,90] and digested as described previously.[30,42,52] All live cells or CD45^{pos} immune cells, were FACS sorted, after exclusion of dead cells with Fixable Viability Dye eFluor® 780 (eBiosciences). Maximum 20,000 immune cells from blood or tissue cells were sorted into Protein LoBind 1.5 ml Eppendorf tube containing 300 μl of RPMI media with 10% of FCS. Cells were loaded onto a Chromium Controller (10X Genomics) for single-cell partitioning, followed by library preparation using Single-Cell 3' Reagent Kits v3.1. For 3 healthy ST and 4 ST from active RA (Figure S1), Totalseq Hashtag were used (Biolegend #394601, #394603, #394605, #394607, #394609) to combine 2 samples per run, and TotalSeq™-A Human Universal Cocktail (V1.0) was used to collect protein expression (CITE-seq) data together with transcriptome data. Single-cell libraries were sequenced on the Illumina HiSeq 4000 sysTem to a minimum depth of 50k reads/cell.

ST-DC index SORT-seq, flow cytometry evaluation of ST-DC subsets' frequency and sorting for the co-cultures with autologous T cells

CITEseq (Figure S3) and our previous data on ST myeloid cells[30] provided surface markers for the gating strategy to evaluate ST-DC subset frequency and sort them for co-cultures with T cells, which was validated in ST-DC index SORT-seq (Figure S4). ST cell suspensions were stained with Fixable Viability Dye eFluor® 780 (eBiosciences) and a CITEseq-guided antibody panel (Biolegend) to identify distinct DC subsets. The gating strategy was based on fluorescence minus one (FMO) and/or unstained controls. Catalogue numbers and fluorochromes of antibodies are provided in the key resources table. Briefly, live cells and then CD45^{pos} cells were gated. In the next step, lineage-positive cells expressing CD3 (T cells), CD19/20 (B-cells), CD15 (neutrophils), CD117 (mast cells), and CD56 (NK/NKT cells) were excluded. Subsequently, cells expressing high levels of HLA-DR or HLA-DR and CD11c were gated. This was followed by gating cells negative for the ST macrophage markers, FOLR2&MerTK. Cells expressing FOLR2 and CLEC10A are CLEC10A^{pos} STM. Gating on FOLR2&MERTK-negative, CLEC10A and CD39&32-positive cells captures all clusters of DC2, DC3 and its iDC3 phenotype, and exclude CD14^{pos}CD16^{pos} tissue monocytes and TNF^{pos}ICAM1^{pos} STMs because they lack or show low expression of CLEC10A and CD32&39. Both DC3 and its iDC3 phenotypes as well as SPP1^{pos} STM clusters express CD9 but SPP1^{pos} STM cluster can be excluded from DCs by the lack of CLEC10A. CLEC10A-positive CD32&39-positive DCs were gated into different subtypes based on the combination of CD1c and CD14 expression: DC2 by high CD1c, iDC3 by low CD1c and high CD14 expression, DC3 by low CD1 and lack of CD14.

To validate this sorting strategy, ST-DC2, DC3 and its DC3 phenotypes, as well as SPP1^{pos} and CLEC10A^{pos} STMs to serve as negative controls, were sorted using Sony MA900 directly into two 384-well plates to perform ST-DC index SORT-seq (a modified version of CEL-Seq2) (Figures S4A and S4B). Library generation and sequencing were provided by Single Cell Discoveries (Utrecht, Netherlands). Read alignment and generation of count matrices from raw data were performed using STAR (v 2.7.11a) pipeline against the Human Genome (GRCh38-3.0.0) and performed UMI counting. The ST-DC index SORT-seq confirmed the accuracy of the ST-DC subset gating strategy (Figure S4C). This gating strategy was used for the co-cultures of ST-DC subsets with PB memory CD4^{pos} T cells, in which T cell phenotypes were evaluated by intracellular cytokine production, and expression of surface costimulatory molecules *(Co-culture-2 below)*. The same gating strategy was also used to evaluate the frequency of ST-DC subsets in synovial biopsies from patients with active RA and RA in disease remission (Figures 1J and 1K). For the initial ST-DC subset/T cell co-culture experiment *(Co-culture-1)*, we used a smaller panel that included markers for the exclusion of lineage-positive cells as above (dump-channel). The STMs were excluded by high surface expression of CD14 that similarly to studies by Cytlak et al.[12] showed at least 1 log higher expression of CD14 compared to ST-iDC3. The accuracy of this initial panel was further confirmed through back validation using ST-DC index SORT-seq (Figure S4D), which shows that inclusion of low and intermediate CD14 expression capture majority of DC3/iDC3 and excludes majority of STMs. To ensure the specific capture of all ST-DCs, CLEC10A positive cells were gated and ST-DC2 were identified by high CD1c expression while DC3/iDC3 were identified by high CLEC10A and low/neg CD1c expression (Figures S7A and S7B).

ST-DC/T cells Co-cultures

Co-culture-1: scRNAseq of T cells. Autologous memory CD4^{pos} T cells were FACS-sorted from PBMCs based on their co-expression of CD3, CD4 and CD45RO. Details of the antibodies used are provided in key resources table. We used CD3 activating antibody to mimic TCR engagement (BioLegend, #300438 clone UCHT1). ST-DC subsets and T cells were sorted into FACS tubes containing complete RPMI1640 medium (10% FCS, penicillin/streptomycin 100U/mL, and 2mM Glutamax). Co-culture was set up when synovial biopsy yielded enough cells at least in one ST-DC subset (minimal 200 cells). Cells were co-cultured at a 1:5 ratio for each DC subset (200-1000 cells) plus memory T cell (1000-4000 cells) in 200μl of X-VIVO 15 Serum-free Cell Medium (BE02-060F, Lonza) supplemented with 2% human serum (H3667, Sigma) or in complete RPMI1640 in a 96-well round-bottom cell-culture plate (3799 – SLS, Corning). After 5 days in culture, the changes in T cell phenotype were investigated using scRNAseq (BD Rhapsody Immune

Response Panel, described in the section below). Data from all co-cultures were used to build a Seurat object of T cells. Subsequently, only those that yielded results from both matched ST-DC subsets (DC2 and DC3/iDC3) were used in the statistical comparison. ***Co-culture-2: Intracellular cytokine staining of T cells.*** Guided by the data from the first co-cultures, we modified culture conditions to better support T cell responses. Briefly, autologous memory CD4^{pos} T cells were enriched via negative selection from PB of RA patients with active disease using the EasySep™ Human Memory CD4+ T Cell Enrichment Kit (STemCELL, #19157), which minimises T cell stress as compared to FACS sorting. Cells were co-cultured with synovial ST-DC subsets sorted according to optimised CITEseq-guided strategy (Figures S3 and S4) in 96-well round-bottom cell-culture plates (3799 – SLS, Corning) in the presence of anti-CD3 at 0.25 μg/ml (to mimic antigen stimulation) (BioLegend, #300438, clone UCHT1) and IL-15 at 20 ng/ml (PEPROTECH, #200-15) to provide a survival signal, at a ratio of 1:5 for 5 days in complete RPMI1640 medium. After 5 days in culture, changes in T cell phenotype were investigated by evaluating the expression of a set of extracellular and intracellular receptors/cytokines and transcription factors by flow cytometry. Details of antibodies are provided in key resources table.

Mapping DC subsets in STs using immunofluorescent staining
Formalin-fixed paraffin-embedded 5μm-thick ST sections were stained with antibodies directed against markers LAMP3 or AXL or CD1c or CD68 or CLEC10A or in combination, or with appropriate isotope control antibodies following previously published protocol.[30] Details of the primary and secondary antibodies used are provided key resources table. The sections were visualised with a Zeiss LSM 880 confocal microscope, using either a water immersion LD C-Apochromat ×40/aperture1aperture1.3, or an oil immersion Plan-Apochromat ×63/1.4 objectives, and images acquired using Zen Black software (Zeiss). All images were processed (brightness/contrast adjustment and background subtraction) using the same software.

The *in vivo* model of disease flare in remission RA
Patient recruitment criteria and the study design of the BioRRA study[58,59] are described briefly in the "patient recruitment and management" section. PBMCs isolated from anticoagulated peripheral blood from n=12 RA patients in sustained disease remission at baseline (at which treatment was withdrawn without tapering) and at the follow-up time point (disease flare or drug-free remission) were isolated by density centrifugation and collected into foetal calf serum (FCS) with 10% DMSO and stored at -150°C. On the day of myeloid cell isolation, PBMCs were carefully defrosted and all live PB myeloid cells were FACS-sorted based on their expression of HLADR and the absence of markers of T-, B- and NK-cells. Details of the antibodies are provided in key resources table. Cells from individual patients were tagged and processed into single-cell libraries using BD Rhapsody sysTem as described in the BD_Rhapsody scRNASeq section.

Sample Preparation for BD Rhapsody scRNAseq of DC-T Co-Culture_1 and BioRRA Cohort and PB DCs
Cells were labelled with unique sample identifier tags (Sample Tag 1-12) using the BD Human Single-Cell Sample Multiplexing Kit (633781/BD Bioscience) according to the manufacturer's protocol. Cells were then loaded onto the scRNA-seq BD Rhapsody Cartridge using the BD Rhapsody Cartridge Reagent Kit (633731) according to the manufacturer's protocol. Single-cell cDNA was prepared using the BD Rhapsody cDNA Kit (633773). This was followed by single-cell Tag library preparation kit (633774) and mRNA library preparation either for the BD Rhapsody Immune Response Panel (633750) (ST-DC/ T cell co-culture / BioRRA Cohort Experiments) or for the BD Rhapsody WTA (633801) (PB DCs). Libraries were sequenced using Illumina NextSeq 500 (Glasgow Polyomics).

Analysis of all Single Cell RNA Sequencing Data
Raw data analysis. Read alignment and generation of count matrices from raw scRNAseq data of 10x Genomics platform was performed using the Cell Ranger (v7.0.0, with parameter "include-introns=false") pipeline. The "cellranger count" tool was used to map the reads against the Human Genome (GRCh38-3.0.0) and performed UMI counting. For analysis of data from BDRhapsody platform, the sequencing reads were processed with BD Genomics Rhapsody Analysis Pipeline CWL (BioRRA cohort and synovial organoid data processed with v.1.0 and DC-T co-culture cohort with v.1.9.1). In some runs of the co-culture cohort where the read2 was too short for the pipeline; two random base-pairs were added. Reads were either mapped against the BD Rhapsody Immune Response Panel reference (BioRRA and Co-culture-1, or against GRCh38.p12 human genome reference (Organoid cohort). For the co-culture cohort, the expected cell number was defined with the "cellNum" parameter as defined in Table S3. The Seurat package (4.0.3) in R was used to create Seurat objects for each dataset (CreateSeuratObject) either from CellRanger output containing the matrix.mtx, genes.tsv (or features.tsv), and barcodes.tsv files from 10XGenomics data or from the RSEC_MolsPerCell.csv file for BDRhapsody data. Ambient RNA was removed using SoupX[67] (1.6.2) from 10XGenomics data. Cells of all datasets were filtered for number genes and UMIs, and those with whole transcriptome for % mitochondrial genes within three median absolute deviation (MAD) around the median population.[91,92] The data was normalized (NormalizeData) and the top 2000 variable genes were identified for all samples (FindVariableFeatures). Cell doublets were marked using DoubletFinder[68] (2.0.3) on single objects, and clusters >25% doublets were removed after integration. Protein level information derived from antibody-derived tags (ADT) were added and normalized using centred log ratio transformation (CLR). Deconvolution of the hashtag/sample information was performed using cellhashR (1.0.3) and Souporcell (2.5) was used to improve the deconvolution using SNPs information. ***General data integration and clustering***. Prior to integration all relevant samples were merged based on common features and re-processed as one Seurat object. The data was re-normalized, adjusting the scale factor to the median number of counts, as provided in Table S2. Principle component analysis (PCA) was performed on identified variable features across all samples (FindVariableFeatures). Cell embeddings from the selected (as given

in Table S2) principal components (PCs) were used in UMAP generation (RunUMAP) to allow for visual inspection of batch separation prior to integration. Integration was then performed using the Seurat wrapper function (RunHarmony, SeuratWrappers, 0.3.0) for Harmony[71] integration (specific versions of harmony used for each integration given in Table S2). Batch variables to be removed by integration and theta values were specified (group.by.vars, theta parameters), as given in Table S2. The resulting harmony-corrected PCA embeddings were then used for UMAP generation, and the selected principal components (harmony-corrected PCs) were visualized (RunUMAP). The same PCs were used to determine the k-nearest neighbours for each cell during SNN graph construction before clustering at the chosen resolution of (FindNeighbors, FindClusters) as in Table S2. Clusters were identified their expression of canonical marker genes (FeaturePlot) and identification of cluster-markers (FindAllMarkers, test.use=MAST). Such cluster markers were identified as genes with significant adjusted p-value of <0.05 (Bonferroni and multiple test correction) and expressed by greater than 40% of cells in the cluster ('min.pct' parameter 0.4). ***Isolation and Identification of PB and ST myeloid DC***. The raw scRNAseq data from PB and ST with 10XGenomics platform were integrated with our previously published myeloid cell data set[30] and a scRNA-seq dataset of 10K healthy PBMCs from 10x Genomics. All previously published data were reprocessed using the same methods described above. Coarse cell types were identified as shown in Figure S1A before all myeloid cell populations (CD14^{pos} monocyte, CD16^{pos} monocyte, broadly annotated ST macrophage and DC) were isolated from integrated PB and ST dataset. Selected cells (n= 70,471) were re-processed with pipeline described above and values supplied in Table S2. Myeloid cell clusters were identified based on previously described nomenclature[30] and clusters found in analyses of PB alone. Next, we investigated which cells cluster with PB DCs and expressed classical myeloid DC markers, including the proteins CD11c and MHC-II as well as genes CLEC10A and CD1c. Clusters with high expression included CD1c^{pos} DCs, CCR7^{pos} DCs, and SDS^{pos}NR4A3^{pos}CXCR4^{pos} tissue DC cluster as well as a population of FOLR2^{high}CLEC10A^{pos} STM. These populations and their potential PB predecessors were highlighted and isolated for further analysis. Selected cells (n= 37,725) were re-processed with same pipeline and re-visualization and clustering of these data identified additional intermediate clusters. We excluded macrophages by high expression of FOLR2 and C1QA RNA. The remaining cells were then isolated (n= 7869) and reanalysed with same methods described above and visualized in Figure 1. Cells were annotated based on trajectory analysis and well annotated DC2, DC3 and iDC3 markers. The exact flow of analysis is described in result section and illustrated in Figure S1. *Isolation and Identification of ST CD4^{pos} T cells.* CD4 T cell, CD8 T cell, and NK populations were isolated from integrated PB and ST dataset. Isolated cells were re-processed with pipeline described above. Contaminant cells were removed based on identified differentially expressed marker genes and samples with fewer than 42 remaining cells were excluded. Preprocessing, integration and clustering was repeated after removal of contaminants. CD4, CD8, and NK clusters were annotated based on differentially expressed marker genes and those annotated as NK or CD8^{pos} T cells were excluded, CD4^{pos} T cells were re-processed and clustered using given parameters (Table S2). Clusters were annotated based on differentially expressed marker genes, as described above, and guided by published ST T cells data sets.[42,52] *Reference annotation.* scRNAseq data of CD4^{pos} T cell from ST-DC co-culture were integrated with the appropriate reference data (ST CD4^{pos} T cells) for annotation of clusters. The appropriate datasets were merged based on common features and integrated using method described above, adjusting the scale factor for normalization (Table S2) to account for read depth differences between platforms/experiments. Integrated clusters were annotated based on reference (ST) dataset clustering, by generating heatmaps of gene expression correlation matrix as well as a confusion matrix, illustrating the proportion of cells from original ST reference clusters within each of the new integrated clusters. *Pathway Analysis.* Pathway activity was inferred across selected ST-DC clusters using PROGENy (v1.24.0) as recommended in package scRNAseq vignette. Briefly, a progeny assay was created in the Seurat object using the progeny function, specifying the top 500 footprint genes per pathway, alongside num_perm=1, and scale=FALSE. The progeny assay scores were scaled using the Seurat ScaleData function. Mean scaled pathway activity was calculated by ST-DC cluster and visualised using the pheatmap package (v1.0.12). Cytokine and Cytokine receptor interaction were investigated in selected DC and CD4^{pos} T cell clusters by looking at genes from the KEGG_Cytokines and cytokine receptors pathway (hsa 04060). Genes from this pathway were specified in the 'features' parameter within the FindAllMarkers function of Seurat (5.0.1). For both DC and CD4^{pos} T cell cytokine pathway analysis, minimum logFC was specified as 0.5, DE genes were to be expressed in minimum 25% of cells in the cluster alongside being positively upregulated in the cluster, and p<0.05 based on MAST with Bonferroni correction for multiple comparison. The same parameters were applied where an individual clusters profile was assessed by synovial disease state. *Cell Trajectory Analysis.* Single-cell trajectory analysis (RNA velocity[75]) of ST myeloid DC and active RA CD4 T cells clusters, and their potential peripheral blood precursors, was performed by estimation of spliced and unspliced counts using the velocyto command line interface (velocyto run10x). Generated.loom files for each sample, containing transcript splicing information, were incorporated into our analysed Seurat object by splitting the object by sample, loading each.loom file using the (ReadVelocity, SeuratWrappers 0.3.0)) and creating a new assay for spliced, unspliced and ambiguous counts before merging our samples back together again, recreating our integrated Seurat object. This Seurat object was then converted for application in python (SaveH5Seurat, Convert) using SeuratDisk (0.0.0.9019) package. The converted.h5ad file can then be read into python using the scanpy[74] (1.9.3) package, which creates an AnnData (0.9.1) object (sc.read). The spliced and unspliced count data was normalized and pre-processed as recommended by scvelo[75] (0.3.1) before running RNA velocity analysis. A PAGA[76] graph was constructed (scv.tl.paga, scv.pl.paga) to illustrate cluster connectivities and RNA velocity is used to infer direction of identified PAGA cluster transitions. Velocity pseudotime was estimated and genes were ranked by velocity to identify top differentially expressed unspliced genes for each cluster (rank_velocity_genes). *Ligand-receptor interaction analysis.* Inference of cellular communication was computed using the CellphoneDB[77] package (v.5.0) using the *cpdb_statistical_analysis_method* ran in Python (v.3.8). The analysis was run using the following constraints; returned ligand/receptor genes must be expressed in at least 10% of all cells in a given cluster, with significant interactions being defined at a p-value of <0.05

after mean expression values of interacting clusters are subject to permutation. All other parameters were run as recommended. Predicted interactions were generated for all cell type clusters in the scRNA-seq dataset followed by a refined analysis limited to co-localised cell types of interest as reported in the spatial analysis. Significant interactions were visualised using the R (v.4.2.2) implementation of ktplots (v2.3.0) and additional custom visualisation scripts. *Predictive Module Score Analysis (BioRRA Cohort).* Annotation of clusters in BioRRA cohort (targeted immune gene panel) was guided by integration with whole transcriptome PB data. Differentially expressed genes upregulated in DC2, DC3, and iDC3 clusters at baseline of patients who go on to flare upon treatment withdrawal were identified using the FindMarkers function (only.pos = TRUE, logfc.threshold = 0.25). This process was repeated for genes upregulated at endpoint flare versus endpoint sustained remission. Shared genes between these two tests were identified for generation of our DC flare-associated module score. To generate this score, the AddModuleScore function from the Seurat R package was utilised with parameters (features=list(DC Flare Associated Genes), ctrl=10, name='DC Flare Module Score', pool=TRUE). This module score was calculated for DC2, DC3, and iDC3 clusters, and mean expression of the module scores by patient and timepoint were utilised in AUC-ROC analyses.

MNP-Verse analysis

We utilized the AddModuleScore function from the Seurat R package to compute module scores for feature expression programs in single cells. The genes belonging to each cluster were selected using the FindAllMarkers function (with parameters ''min.pct = 0.4, logfc.threshold = 0.7, test.use = "MAST", only.pos = T"). Subsequently, the score for each cluster was computed and integrated into the MNPverse Seurat object, and scores for the ST-DC2 LAMP3^{pos}CCR7^{pos} were visualised. Harmony (1.2.0) integration of our myeloid cell dataset from RA PB and ST with MNPverse dataset was performed. Common features between the two datasets were selected, and we used the median number of counts for scaling factor for normalization. We corrected for batch variables including sample donor, experimental differences, and tissue variations within the dataset (group.by.vars=c("Unique_ID","Experiment","Tissue"), theta=c(0,10,0)).

Mapping of ST myeloid DC in situ with CosMx single cell spatial transcriptomics

We used the Nanostring CosMx Spatial Molecular Imaging platform to measure expression of 960 genes discriminating transcriptional profiles and spatial localization of 127,199 cells (69 fields-of-view (FOV)) in paraffin-embedded synovial biopsies from 3 active naive to treatment and 3 RA patients in sustained clinical and imaging remission (~11 FOV per donor). Demographic, clinical and immunological characteristics of enrolled patients as well as synovitis degree of corresponding STs are described in Table S1. *Cell segmentation.* Initial image segmentation was performed with Mesmer[49] with the following parameters: mesmer_mode = "both", scale = pixel size of the images. We used the cell boundaries estimated by Mesmer as a prior for refinement of the segmentation with Baysor[50] based on transcript densities, using the R wrapper (https://github.com/korsunskylab/baysorrr). Following successful cell assignment, we generated a gene-cell expression matrix and performed quality control, removing any cells with less than 30 counts and/or expression of less than 20 genes. Additionally, cells with radius less than 2 μm were also removed. Cells which passed QC filtering were then annotated using pipeline for cell type labelling described in Chen et al.[93] *Coarse cell type annotation.* Briefly, read counts were normalized and log-transformed to median total counts of all cells remaining after filtering. PCA was performed and embeddings were corrected by integration with Harmony[71] (0.1.0), specifying sigma value of 0.25 and theta values of 0 for both, sample run and FOV batch variables. Harmony corrected PC-embeddings were used to generate two-dimensional UMAP[94] (uwot 0.1.16) and cell clusters were identified by shared nearest neighbour (SNN) modularity clustering. Clusters of coarse cell types were annotated based on marker genes identified by differential expression analysis performed using presto wrapper (1.0.0, https://github.com/immunogenomics/presto/tree/glmm/) for Generalised Linear Mixed Model (GLMM) estimation with lme4 (1.1-34) as described in Chen et al.[93] Genes were considered significant when adjusted p value was less than 0.01 and an average logFC more than 0.5. *Preparation of scRNAseq for reference annotation of spatial data.* Following coarse cell type annotation, CosMx data were integrated with our ST scRNAseq dataset for reference annotation of subclusters. In preparation for this, our ST scRNAseq dataset was refined by removing genes that are not present in the CosMx SMI gene (n=922) panel. The data were then re-filtered to remove cells that now have low number of counts/features due to reduced gene panel. Variable features were identified, and the data was renormalized, adjusting the scale factor to account for reduced number of counts (median = 1255). We then followed standard pipeline for Seurat pre-processing and clustering of scRNAseq data, as described above, for coarse cell type annotation. Coarse cell type populations of interest were isolated, and as before, data was re-integrated, a new UMAP generated, and re-clustered with reduced gene panel. Any clusters that were indistinguishable with CosMx gene panel were removed. Relevant genes for population of interest arranged by z-score (presto, 1.0.0) and we ran sensitivity analysis by running the pipeline for integration and clustering using from 50–900 genes top variable genes and selecting the minimum number of genes necessary to distinguish our described DC and T cell subsets. We then harmonized and clustered with minimum relevant genes selected from sensitivity analysis and annotated clusters based on correlation of gene expression with original annotations. Cells with clashing labels were removed and the number of cells per cluster was down sampled to median number cells per cluster. *Reference annotation of CosMx spatial data with refined scRNAseq data.* Each population of interest (Myeloid, Stromal, Endothelial and T Lymphocyte) from the spatial data was isolated based on coarse cell type annotation for integration with the appropriate scRNAseq reference. CosMx data was reduced to genes selected from sensitivity analysis in preparation of scRNAseq reference for that cell type. This allowed us to minimize noise and focus only on minimum genes necessary to define clusters. The data was then merged and renormalized adjusting the scale factor to account for reduced number of counts between both CosMx and scRNAseq dataset before following standard

harmony pipeline for integration across modalities, accounting for source of the data (spatial/scRNAseq, theta=2) and sample ID (donor/sequencing run, theta=0) as batch variables. The integrated dataset was then re-clustered and new integrated clusters were identified. To do so, a heatmap of correlation matrix comparing the marker genes of new clusters with marker genes of the original single cell clusters was visualized. We also generated a confusion matrix – a heatmap illustrating the frequency of cells from original single cell reference clusters within each of the new integrated clusters. In the case that the new integrated cross-modality clusters contained multiple of scRNAseq reference clusters we performed subclustering and revisualization of gene correlation matrix and confusion matrix. Fractions of cells of each cluster from different sources was also visualized as stacked bar plot to identify any populations unique to CosMx spatial technology. The new integrated clusters were automatically reference annotated using the gene correlation matrix, annotating new clusters with the name scRNAseq reference cluster with the highest correlation of gene expression. This reference annotation was also performed manually, and results compared to finalize annotations before transferring new cell labels. Once all coarse cell populations of interest in spatial transcriptomic were isolated, integrated with scRNAseq reference, re-clustered and annotated, the new fine type cell annotations were transferred to the original CosMx spatial dataset containing all cell types. Spatial localization of coarse and fine type cell annotations were plotted using ggplot2 (geom_sf) allowing for visualization of cell geometries identified from segmentation (described above) manipulated using sf package (1.0.16).

Niche and colocalization analysis of CosMx spatial transcriptomic data

To do spatial segmentation we first identify low-quality regions within the tissue, performing the following steps: (1) FOV region annotation and gridding, (2) spatial smoothing, and (3) dimensional reduction and clustering. ***FOV region annotation and gridding.*** We gridded the cellular region of each FOV by performing Voronoi tessellation on the cell centroids with the FOV boundary as the bounding box. Voronoi tessellation divides the space such that:

$$Distance\ (PVk, Ci\ =\ k) \le Distance(PVk, Ci, i \ne k)$$

where PVk is any point P(x,y) in the Voronoi region Vk, and Ci is the centroid of the Voronoi region Vi. Because Voronoi tessellation grids the whole FOV irrespective of empty spaces within the tissue, we chose to perform Voronoi tessellation only between cells that are less than 50 μm apart from at least one other cell. Cells that are over 50μm apart from other cells are included in the analysis but with their original cell polygons instead of Voronoi regions. For most of the FOVs, we observed a gap between the last layer of cells and the FOV boundary. This led to edge effects where the cells closer to the edges had elongated shapes. To correct this, we changed the shapes of Voronoi regions of the edge cells to an intersection between a circular buffer of 15μm from the cell centroid of the boundary cells and the corresponding Voronoi region. This marked the end of gridding of the cellular region of the tissue. We merged all the Voronoi regions in each FOV and annotated it as "tissue". We determined "glass" regions in each FOV by finding the non-intersecting region between the bounding box of the FOV and a 30μm buffered tissue region of the FOV. We buffered the tissue region to ensure we didn't capture probes in the boundary regions between glass and tissue. Our rationale behind ignoring boundary transcripts is that these probes could belong to cells but were not assigned to cells due to segmentation errors. Grouping these into "glass" regions could skew our background identification. We then tiled the glass region of the FOV into 4-sided polygons that contain the same number of transcripts as the mean number of transcripts per Voronoi region in that FOV. ***Spatial smoothing.*** To construct the gene expression matrix of the tissue region, we mapped only the transcripts (both positive and negative probes) assigned to cells during segmentation to Voronoi regions. Because negative probes are excluded during cell segmentation, we assigned negative probes to cells by assigning a cell ID to a negative probe if it was within a cell boundary and 0 otherwise. To construct the glass region's gene expression matrix, we used the "st_intersect" function to map transcripts to the glass tiles. We then combined both expression matrices to build a gene-polygon matrix for each FOV. From this point on, we will refer to both the Voronoi regions and the glass tiles as "polygons" and original cell shapes as "cell polygons". To perform spatial smoothing, we ensured each cell captures a fraction of its neighbors (in addition to all transcripts from itself) in a diffusion-based method controlling for how aggressively we borrow transcripts (l) from our neighbors and how many degrees of neighbors we want to borrow transcripts from (k). The first step of spatial smoothing is to construct an adjacency matrix. We did that by constructing an unweighted Delaunay graph on the polygon centroids and pruning the edges between tissue and glass polygons. Pruning is important because our goal was to identify regions in the tissue that have similar gene expression profiles as glass, and borrowing transcripts from glass would make some tissue regions look like glass because of smoothing and not because they are low quality. After calculating the adjacency matrix, we smoothed it by diffusion process where the smoothed matrix M is calculated as:

$$M\ =\ (I+lA)^k$$

Where I is the Identity matrix, l is the rate of diffusion, A is the adjacency matrix, and k is the number of steps of diffusion. We row-normalized the smoothed matrix and built the smoothed gene expression matrix (G) as:

$$G\ =\ G_{raw} * t(M)$$

Dimension reduction and clustering

We then performed log-normalization, scaling, weighted-PCA, Harmony to correct for batch effects (sigma = 0.2, batch variables = SampleID, SampleFOV, nPCs = 20), UMAP, and clustering as described in the cell type labeling section to identify the tissue regions clustering with glass regions. These regions were labeled "low-quality" regions and removed from the analysis. ***Region annotation.***

To identify regions, we perform spatial smoothing, dimension reduction and clustering as described above on high-quality tissue regions. Clusters are annotated based on their cell composition. Furthermore, we performed colocalization analysis to define organization of cell subsets within the described tissue niches. Applying a permutation approach, as in Chen et al.,[93] we identified nearest neighbours and then randomized the positions of cells surrounding the defined cell type of interest and determined whether or not the colocalization of two subsets was not expected by chance. Significant colocalizations (adjusted p value < 0.05) were plotted as Z-score.

PRIME cells data set analysis

The PRIME cell data set[60] encompasses over 364 time points, both preceding and during eight flares, spanning a period of 4 years. Samples from this dataset which had conflicting metadata information or did not have information denoting weeks to flare were excluded. Raw readcounts were loaded and analysed using DESeq2 (1.40.2), transformed with VST, batch effects were evaluated using PCAtools (2.12.0) and readcounts were adjusted to remove batch of sequencing and occurrence of flare timepoint batch effect using Combat/SVA (3.48.0).

MIR155 expression and experimental overexpression of MIR155 in ex-vivo peripheral blood (PB) DC2 cells

MIR155 expression. DC2 from healthy and active RA PB, and ST from active RA were sorted based on negative expression of cell lineage markers (CD3, CD19/20, CD56, CD15 and CD117) and high expression of CD1c into tubes with microRNA preservation buffer from miRNeasy micro-Kit (217084, Qiagen). Clinical information for these patients is in Table S1. To evaluate MIR155 and housekeeping control, RNU6 expression, RNA was transcribed into cDNA and amplified with miScript Reverse Transcription Kit II (218161, Qiagen) and miScript PreAMP PCR Kit (331451, Qiagen), respectively. The miScript primer assays (Qiagen) were used for semi-quantitative determination of expression of U6B snRNA (MS00033740) and MIR155 (MS00031486) in combination with miScript SybR Green PCR kit (1046470, Qiagen). The expression of genes of interest was presented as a relative value $2^{-\Delta CT}$, where ΔCt is the Ct (Cycle threshold) for RNU6 (housekeeping genes) minus the Ct for the gene of interest. ***Ex-vivo MIR155 overexpression.*** DC2 (CD1c^{high}) from PB of active RA patients (n=12) were FACS-sorted into tubes with complete RPMI1640 media and seeded overnight in flat bottom 96-wells plates at a density of 10×10^3 cells/well. The next day, cells were transfected using the Dharmafect 3 transfection sysTem (T-2003-02, lot 00662107, Dharmacon) with either hsa-miR-155 mimic (C300647-05-305, lot 180510, Dharmacon), negative control miRNA mimic (CN-001000-01-05, lot 2145003, Dharmacon), or negative control labelled with 20nM Dy547 fluorochrome (CP-004500-01-05, lot 2054853, Dharmacon). After 4h, cells were either left unstimulated as controls, or were stimulated with LPS (100ng/mL, L6529, Sigma) for 48h. Culture supernatants were collected for soluble mediator analysis. Transfection efficiency was estimated based on the proportion of cells that were successfully transfected with the Dy547 mimic, and experiments where the transfection efficiency was below 60% were discarded. Cytokine concentrations in the culture supernatants of the RA DC2 were quantified using a predesigned high-sensitivity Luminex 100^{TM} Multiplex Kit (Millipore UK) on a Bio-Plex sysTem (Bio-Rad).

Phenotyping DCs in mesenteric lymph nodes (mLN) in wild type and miR-155 gene deficient mice

The mesenteric lymph nodes (mLN) from 8–12-week-old C57BL/6J (WT) and congenic Cg-Mir155tm1Rsky/J (miR-155 deficient) were harvested and digested with 1mg/mL of Collagenase D for 40 min in a 37°C shaking incubator at 150 RPM speed. After neutralisation of collagenase with complete media, cells were incubated with antibodies indicated in key resources table for 30min at 4°C and acquired by FACS AriaIII. Data was analysed using FlowJo (Version 10.7.1).

Isolation and analysis of mouse DC2 from gut, lymph and draining lymph nodes

To obtain thoracic duct lymph, mesenteric lymphadenectomy was performed on 6-week-old male C57/Bl6 mice by blunt dissection at laparotomy. The thoracic lymph duct was cannulated with a polyurethane cannula (2Fr). Lymph was collected in PBS / 20 U/mL of heparin sodium on ice, overnight as we described previously.[65,95] Matched small intestine was isolated and digested as described previously.[65,95] Lymph DC2s were identified as MHC II^{hi} CD11c$^+$ B220$^-$ CD11b$^+$. In the mLN and intestine, cDC2s were identified as F4/80^{lo} MHC II^{hi} CD11c$^+$ CD11b$^+$. DC2 from different compartments were sorted (>100,000 cells). Information on antibodies used is provided in key resources table. RNA was isolated using RNAeasy kit (217084, Qiagen). BulkRNAseq on cells isolated from lymph, intestine, and mesenteric lymph node was carried out as described previously and available under GSE160156.[65]

QUANTIFICATION AND STATISTICAL ANALYSIS

Statistical analysis was performed using Prism 10 (GraphPad Software). Statistical significance was evaluated by T test/Mann-Whitney or One-way ANOVA/Kruskal-Wallis with correction for multiple. The exact details on statistical methods are provided in each Figure legend and in the scRNAseq method sections above.